Evolution of a structural basin: Numerical modelling applied to the Dehdasht Basin, Central Zagros, Iran

Kobra Heydarzadeh[1, 2], Jonas Bruno Ruh[2, 3], Jaume Vergés[2], Hossein Hajialibeigi[1], Gholamreza Gharabeigli[4]

[1] Department of sedimentary basin and petroleum, Faculty of Earth Sciences, Shahid Beheshti University, Iran

[2] Group of Dynamics of the Lithosphere (GDL), Institute of Earth Sciences Jaume Almera, ICTJA-CSIC, Barcelona, Spain

[3] Geological Institute, ETH Zurich, Switzerland

[4] National Iranian Oil Company, Exploration Directorate

Corresponding author: Kobra Heydarzadeh (k_heydarzadeh@sbu.ac.ir),

Abstract

The Dehdasht Basin, a small structural basin located in the southeast of the Dezful Embayment in the Zagros fold-and-thrust belt, has a complex tectonic structure characterized by both compressional and halokinetic features. 2D numerical models are used to test how geometrical and rheological parameters affected the Miocene-Pliocene evolution of this deep basin. The analysed parameters include rate of syntectonic sedimentation and erosion, thickness and viscosity for the lower detachment (Hormuz salt) and for the upper detachment (Gachsaran evaporites) developing diapiric salt walls, salt extrusions and minibasins-growth synclines that characterize the internal structure of the Dehdasht Basin. Assuming reasonable dimensions and rheologies (0.5 km Hormuz basal detachment with moderate viscosity of 10^{19} Pa·s, and Gachsaran upper detachment with a minimum original thickness of 1.5 km and viscosity between $5 \cdot 10^{18}$ and 10^{19} Pa·s), our models reveals that an almost intermediate ratio between the rates of surface processes and deformation well approximate the geological and geophysical observations. A local decrease in the thickness of the Hormuz salt below the Dehdasht Basin with respect to surrounding regions was of great importance for its structural evolution. We suggest that the large volume of ~~the~~ Gachsaran evaporites presently filling the basin was partly due to their gravitational flow from the emerging surrounding anticlines into the basin. The numerical experiments also demonstrate that in a compressional setting, shortening is the main factor for the rapid initial growth of the diapirs, although, with increasing syntectonic sedimentation the effect of shortening diminishes.

Keywords: Dehdasht Basin; Numerical modelling; Shortening and diapirism; Minibasins; Detachment levels; Zagros fold-and-thrust belt

1. Introduction

Piggy-back or wedge-top basins are small structural basins which form within active thrust wedges usually infilling elongated growth synclines (Decelles and Giles, 1996; Ori and Friend,1984). Examples of well-studied structural basins are the Axhandle basin in Central Utah (Talling et al., 1995), the Didid Shiraki Basin in the Kura foreland fold-and-thrust belt of the Lesser Caucasus orogenic belt (Alania et al., 2015) or the Tremp-Graus-Ainsa Basin in the South Pyrenees (Chanvry et al., 2018). Sub-basins with different structural or sedimentary characteristics may also form due to the reactivation of pre-existing basement faults in fold-and-thrust belts (Lacombe and Bellahsen, 2016). One such example is the Dezful Embayment in the Zagros fold-and-thrust belt (Bahroudi and Koyi, 2004; Sepehr and Cosgrove, 2007, 2004; Sherkati et al., 2006), which is the focus of our study.

The presence of salt-bearing layers within structural basins significantly affects their structural evolution, especially during shortening and tectonic inversion (Jackson and Hudec, 2017). Halokinetic processes driven by overburden load on the adjoining salt source or by external forces such as horizontal shortening may enhance density-driven salt diapirism triggering minibasin subsidence (Hudec et al., 2009). Diapir-minibasin systems form in several different geological settings, and during both extensional and compressional tectonic regimes. For example, they have been observed in passive margins (the Gulf of Mexico (e.g., Worrall and Sneslson, 1989), the Angolan Margin (Fort et al., 2004; Martori et al., 2000) and the Campos and Santos Basins in offshore Brazil (Demercian et al., 1993)), in intra-continental basins (the Precaspian Basin in Kazakhstan (Volozh et al., 2003)), and in foreland fold-and-thrust belts (the Zagros (Callot et al., 2012) or the Central Sivas Basin in Turkey (Kergaravat et al., 2016; Legeay et al., 2019)). The influence of shortening on pre-existing diapirs has been constrained in several previous studies (Callot et al., 2012; Kergaravat et al., 2017; Vendeville and Nilsen, 1995), and the relationship between compression and resulting structures is well understood.

However, the contribution of salt tectonics to resulting structures is more difficult to evaluate due to the coeval interplay of multiple deformation mechanisms. In particular, there is still a lack of knowledge about the syn-kinematic formation of minibasins during contribution of shallow salt tectonics and shortening. Improved evaluation of the salt tectonics component is a major motivation of this study.

In this study, we focus on the Dehdasht structural basin, a lowland area located in the southern Dezful Embayment (Figs 1). The Dehdasht Basin is bounded by well-developed and high-elevation NW-SE trending anticlines detached above the Hormuz evaporites (Lower Mobile Group) and exposing Cretaceous and Oligo-Miocene limestones (Sarvak and Asmari limestones, respectively). The anticlines have a steep geometry, defined by sub-vertical axial planes and shallowly plunging fold axes. The basin contains several small synclines, filled by Neogene Mishan marine and Aghajari-Bakhtyari non-marine deposits that are bounded by narrow ridges of Miocene Gachsaran evaporites (Upper Mobile Group) (Fig. 2). These synclines as well as the larger-scale surrounding anticlines are sub-parallel to the NW-SE Zagros trend. The diapiric anticlines and synclines are asymmetric and separated by thrust faults, therefore clearly having formed during tectonic convergence (Fig. 2). However, almost rounded synclines enclosed by Gachsaran evaporites in the northwest of the Dehdasht Basin underline the importance of salt tectonics during their development (Fig. 2a).

Here, 2D numerical modelling has been applied to determine the contributions of different mechanisms involved in the evolution of the salt-rich Dehdasht Structural Basin. The importance of surface processes such as variation of sediment flow as well as parameters of the saline unit including the mechanic properties of the both basal Hormuz salt and upper Gachsaran detachments have been tested.

2. Geological setting of the Dehdasht Basin

The Zagros fold-and-thrust belt extends over ~2000 km from the Makran subduction zone in the southeast to the East Anatolian Fault in the northwest (e.g., Mouthereau et al., 2012; Vergés et al., 2011b). The uplift of the Zagros Mountains results from the continental collision between the Arabian and Eurasian plates following a long period of NE-dipping subduction of the Neo-Tethys Ocean since Late Triassic or Early Jurassic times (e.g., Agard et al., 2011). The Zagros fold-and-thrust belt is transversely divided into two tectono-stratigraphic zones, the High Zagros (Imbricate Zone) in the NE and the Zagros Simply Folded Belt (ZSFB) in the SW, separated by the High Zagros Fault (Fig. 1; Berberian, 1995; Sattarzadeh et al., 2002; Sherkati and Letouzey, 2004). The ZSFB developed mainly during Neogene times with a deformation front migrating progressively towards the SW (Hessami et al., 2001; Homke et al., 2004; Khadivi et al., 2010; Ruh et al., 2014; Vergés et al., 2019). In map view, the ZSFB is characterized by two structural arcs, the Pusht-e Kuh arc (Lurestan province) in the NW and the Fars arc in the SE (Fig. 1). The two tectonic arcs are separated along strike by the Dezful Embayment (Fig. 2A).

The Dehdasht Basin in the southern Dezful Embayment was named the Dehdasht Embayment by Sepehr and Cosgrove (2007). These authors proposed that the segment of the Mountain Front Flexure (MFF) running beneath the Kuh-e Siah anticline, to the NE of the Dehdasht Basin, is connected to another segment located beneath the Mish anticline in the south. More recently, these two segments of the MFF are interpreted as connected by the N-S trending oblique and blind Kharg-Mish Fault (Narimani et al., 2012), bounding the closely spaced anticlines to the east (Fig. 2A). The Kharg-Mish Fault is recognized by changes in the thickness of the Cretaceous strata (Sherkati and Letouzey, 2004; Sepehr and Cosgrove, 2007) and could represent an inherited transfer fault separating different segments of the Arabian margin during the Mesozoic, reactivated during Neogene times (e.g., Navabpour et al., 2014). The NW boundary of the Dehdasht Basin is limited by the SE-dipping terminations of the Siah, Kuh-e-Sefid and Bangestan anticlines (Fig. 2A). The non-aligned SE terminations of these two anticlines make it more difficult to relate them to a blind fault at depth. Furthermore, the Khaviz anticline forms the southern boundary of the basin where it is potentially affected by the surface trace of the MFF (e.g. Berberian, 1995) (Fig. 2).

The internal structure of the 1,736 km^2 Dehdasht Basin (56 km in length by 31 km in width) is composed of elongated (8-26 km long) and narrow (2.5-6.5 km wide) synclines filled up of Mishan and Aghajari-Bakhtyari deposits, mostly with NE-tilted limbs and separated by long and continuous Gachsaran evaporitic ridges. In the central and SE of the basin, the narrow synclines are trending NW-SE, parallel to the larger surrounding anticlines (Fig. 2A). The evaporitic ridges, located in the centre and the East, have diverse SW-verging extrusions overlaying the adjacent synclines. Towards the NW of the Dehdasht Basin, the structure mainly consists of Gachsaran evaporites exposing two small rounded synclines of the overlying strata (Fig. 2A). Line length restoration within the Dehdasht Basin at the level of the Competent Group layers shows a horizontal shortening of 8–10 km (17-22%) that is compatible with results from the previous studies in the Dezful Embayment (Sherkati et al., 2006; Najafi et al. 2018). Furthermore, area-balanced restoration suggests that the Gachsaran evaporites in the Dehdasht Basin are more than two times thicker than in the surrounding regions. This large change in stratigraphic thickness may be the result of viscous flow of the evaporites towards the centre of the Dehdasht Basin during its development, as proposed at a regional scale by Sherkati et al. (2005).

The Dehdasht Basin evolved under compression and coeval diapirism, triggered by a thick evaporitic layer (the Gachsaran Formation) between competent layers below and syntectonic clastic deposits above, similar to other examples such as La Popa Basin in NE Mexico (Rowan et al., 2003), the Sivas Basin in Turkey (Ringenbach et al., 2013) or Axel Heiberg Island in

Canada (Harrison and Jackson, 2014). Diapirism within the Zagros fold belt is mostly observed in the SE Fars region where a large number of Hormuz salt diapirs are cropping out (e.g., Callot et al., 2012; Jahani et al., 2009) but very little is known about diapiric structures developed in the Gachsaran evaporites (O'Brien, 1950; Bonini, 2003; Edgell, 1996; Najafi et al., 2018; Sherkati et al., 2005).

3. Regional stratigraphy

In this section we discuss about the diverse sequence of sediments which generally form the Dezful Embayment and the Dehdasht Structural Basin. The stratigraphic succession of the Dezful Embayment is divided into five groups according to their mechanical behaviour (Fig. 3; O'Brien, 1950, 1957): (1) The Basement Group (Pan-African crystalline basement), (2) the Lower Mobile Group (Hormuz salt), (3) the Competent Group (Cambrian to Lower Miocene platform sediments), (4) the Upper Mobile Group (Miocene Gachsaran salt) and (5) the Passive Group (Miocene to recent Aghajari and Bakhtyari fluvial-alluvial foreland deposits).

The most important detachment levels in the Zagros fold-and-thrust belt correspond to the Hormuz and Gachsaran salt levels. The Miocene Gachsaran evaporitic formation (Upper Mobile Group) when thick enough constitutes a decoupling level between the Competent and the Passive Groups as observed in seismic lines (e.g., Abdollahie Fard et al., 2011; Najafi et al., 2014). Less important levels are found intercalated within the Competent Group such as the Late Triassic Dashtak evaporites (e.g., Sepehr et al., 2006; Sherkati et al., 2006).

The Dehdasht Structural Basin is filled by the Gachsaran, Mishan, Aghajari and Bakhtyari successions, collectively termed the Fars Group (Fig. 3). The uppermost part of the Competent Group interbedded with shale and marl layers of the Garau, Kazhdumi and Pabdeh-Gurpi formations is exposed along the surrounding structures. These shale and marl deposits are considered to represent potential intermediate detachments in the Dezful Embayment as described in (Abdollahie Fard et al., 2006; Derikvand et al., 2018; Sherkati et al., 2006) (Fig. 3).

The oldest rocks in the Dehdasht Structural Basin are Early Cretaceous in age. To complete the stratigraphic column of the Dehdasht Basin down to the basal detachment, previous studies from the Dezful Embayment such as Alavi (2007) and Sherkati et al. (2006) were used. The sedimentary sequence from Permian to Jurassic is mostly composed of dolomite and limestone with layers of evaporites from which Triassic evaporites of the Dashtak Formation conform an excellent detachment causing disharmonic features especially across the Bangestan anticline (Sherkati and Letouzey, 2004). From middle Cambrian to lower Permian, the sedimentary sequence contains mostly sandstone and shale (Fig. 3). At the base of the sedimentary cover succession, it is assumed that the Cambrian Hormuz salt (or an equivalent basal detachment level) can have enough thickness to represent an efficient detachment at the basement-cover interface. Its stratigraphic thickness is proposed to be more than 1 km in the Zagros Mountains and ~2.5 km in the Persian Gulf (Edgell, 1996).

4. Numerical model

The numerical experiments conducted in this study are focused to reproduce the tectono-sedimentary interplay observed in the Dehdasht Basin where Gachsaran diapirism occurred after the initiation of shortening.

4.1. Governing equations and rheological implementation

The mechanical model is based on the equations for conservation of mass and momentum for incompressible conditions:

$$\frac{\partial u_i}{\partial x_i} = 0 \qquad (1)$$

$$-\frac{\partial P}{\partial x_i} + \frac{\partial \tau_{ij}}{\delta x_j} = \rho g_i \qquad (2)$$

where u_i is velocity, x_i and x_j are spatial coordinates, P denotes dynamic pressure (mean stress), τ_{ij} are deviatoric stresses, ρ and g_i stand for density and gravitational acceleration, respectively. In order to solve these equations, a two-dimensional finite-difference numerical code (Ruh, 2017; Ruh and Vergés, 2018) is applied. The governing equations (1 and 2) are discretized by a fully-staggered non-deformable Eulerian grid and the system of equations is solved by MATLAB's “backslash” direct solver. Material properties are assigned to Lagrangian markers advecting freely according to the Eulerian velocity field.

Rheology of the applied materials is considered to have a Maxwell-type visco-elastic stress-strain relationship:

$$\dot{\varepsilon}_{ij} = \frac{1}{2\eta}\tau_{ij} + \frac{1}{2G}\frac{D\tau_{ij}}{Dt} \qquad (3)$$

where G is the shear modulus and η the effective viscosity. The shear modulus is set to 100 GPa for all rocks in all simulations and effective viscosity is fixed to range between 10^{17} and 10^{25} Pa·s. $\frac{\mathrm{D}\tau_{\mathrm{ij}}}{\mathrm{Dt}}$ indicates the co-rotational time derivative of the deviatoric stress tensor due to rigid body rotation of materials:

$$\frac{D\tau_{ij}}{Dt} = \frac{\tau_{ij} - \tau_{ij}^{old}}{\Delta t} \qquad (4)$$

Brittle/plastic rheology is implemented by the Drucker-Prager yield criterion, which defines the yield stress σ_y depending on the friction angle ϕ and the cohesion C:

$$\sigma_y = P \cdot sin\varphi + C \cdot cos\varphi \qquad (5)$$

Brittle/plastic yielding applies when the second invariant of the stress tensor exceeds the yield stress locally (F>0):

$$F = \tau_{\mathrm{II}} - \sigma_y \qquad (6)$$

where

$$\tau_{\mathrm{II}} = \sqrt{\frac{1}{2}\tau_{ij}^2} \qquad (7)$$

4.2. Geometrical setup

The geometrical model setup is defined by a box with a length of 80 km and a height of 15 km with a numerical resolution of 401 to 76 nodes, respectively (Fig. 4). Each nodal cell contains 16 Lagrangian markers. Despite much larger than the actual width of the natural prototype, the length of 80 km was chosen because it allows the development of two anticlines with ~30 km wavelength after about 20% shortening (see Fig. 2). The Dehdasht Basin contains a thick sedimentary pile with several intermediate detachments however, for simplicity in the modelling a thinner sedimentary sequence containing one intermediate detachment is used. A thickness of 7 to 8.5 km (depending on the model) is considered for the modelling sedimentary sequence which represents the proposed thickness of the undeformed Zagros sedimentary sequence (Alavi, 2007; Lees, 1952). It consists of two competent layers, corresponding to the Competent Group of the Dehdasht Basin from lower Miocene down to Lower Cambrian (Fig. 3), with a density of 2700 kg/m^3 and an initial viscosity of 10^{25} Pa·s and three relatively weak detachment levels with a density of 2200 kg/m^3 and viscosities of 10^{18}–10^{20} Pa·s (depending on the model; Table 1). According to the Dehdasht Basin, the three mobile levels represent the basal detachment (corresponding to the Cambrian Hormuz Salt or its equivalent), an intermediate detachment (corresponding to the Triassic evaporites of Dashtak Formation or the Lower Cretaceous shale of Garau Formation) and an upper detachment (corresponding to the Miocene Gachsaran salt layers). The lower and upper competent layers as well as the intermediate detachment exhibit thicknesses of 3, 2 and 0.5 km, respectively, for all experiments. However, thicknesses of the lower and upper detachments vary between 0.5–1.5 km (Table 1). A thickness of 1 km is considered for the upper detachment of the reference model. The undeformed sedimentary sequence is overlain by a sticky-air layer with a viscosity of 10^{17} Pa·s and a density of 1 kg/m^3. The application of a sticky-air layer mimics a quasi-free surface along the rock/air interface imposing negligibly low shear stresses (Crameri et al., 2012).

4.3. Boundary conditions and surface processes

Horizontal shortening is imposed by a negative constant velocity of v_x = -0.01 m/yr on the right side of the model box (Fig. 4). On the left side, zero horizontal velocity (v_x = 0) prohibits material to move across the boundary. Both lateral boundaries prescribe free-slip vertical movement. At the bottom, increasing horizontal velocities (v_x = 0, 0.005 and 0.01 m/yr) are applied and separated by two singularity points at x = 25 km and x = 65 km to force the localization of anticline uplift. Vertical velocity at the base is zero. The top of the model is a free-slip boundary with a vertical velocity assuring the conservation of volume within the model box calculated as:

$$v_y = v_x \cdot (Ly/Lx) \qquad (8)$$

where v_y is the vertical velocity along the top boundary and Lx and Ly denote the width and height of the Eulerian model box. Boundary conditions are equal for all simulations.

Surface processes simulating syntectonic sedimentation and erosion are applied by diffusion of the surface line according to:

$$\frac{\partial h_s}{\partial t} = \kappa \cdot \frac{\partial^2 h_s}{\partial x^2} \qquad (9)$$

where κ denotes the diffusion constant, h_s the surface topography and x the spatial coordinate. Free-slip boundary conditions are applied for both left and right sides of the surface. After diffusion of the surface line, erosion is applied by converting rock markers above the diffused line to sticky-air markers. Sedimentation denotes the conversion of sticky-air markers below the diffused surface line to rock sediment markers with a constant density of 2600 kg/m^3 and an initial viscosity of 10^{25} Pa·s (Table 1). Both sedimentation and erosion are applied individually and can therefore depend on separate different diffusion coefficients. In experiments presented here, values for surface diffusion range from 10^{-6} to 10^{-5} m^2/s for both sedimentation and erosion (Table 1).

4.4. Applied rheological and surface process parameters

Seven different series of experiment, including the reference model, have been designed to investigate the role of syntectonic surface processes and variable thickness and strength of the different detachments on the development of a structural basin (Table 2). Reference model 1 exhibits thicknesses of 1.5 km and 1 km for the lower and upper detachment, respectively, and a viscosity of $\eta = 10^{19}$ Pa·s for each of the detachment levels. Viscosity of 10^{19} Pa·s is in agreement with the value for the Newtonian salt layers in the numerical modelling (Chemia et al., 2008) and also with the average value for the Hormuz salt (Mukherjee et al., 2010). Furthermore, surface processes of the reference model 1 have equal diffusion coefficients for both sedimentation and erosion of $\kappa = 2 \cdot 10^{-6}$ m^2/s. All presented model series focus on the effect of one parameter while other parameters will remain equal to the reference model (Table 2). Model series 2 and 3 test the effects of varying surface process intensity. Model series 4 and 5 investigate the influence of stratigraphic thicknesses of the basal and upper detachment levels. Model series 6 and 7 examine the impact of detachment strength imposed by variable viscosities.

4.5. Limitations of the model

Numerical experiments use several simplifications when simulating the conditions and rheological properties of natural systems. For example, the applied numerical code is defined in two spatial dimensions, while deformation, in particular salt activity (i.e., in the Dehdasht Basin) is a three-dimensional process, i.e. salt flow from or into the section is considered negligible in the models of this study. Another limitation is the fixed singularity points applied to the models to force the formation of the large boundary anticlines of the Dehdasht Basin. In spite of Sepehr and Cosgrove (2007), Bahroudi and Talbot (2003b) and Ahmadhadi et al. (2007) who suggest the existence of basement faults to the south of both Kuh-e-Siah and Khaviz boundary anticlines, there is no data about their activity during Miocene folding in the Dehdasht Basin. However, Ahmadhadi et al. (2007) propose early reactivation for basement faults in the central Zagros before the main Mio-Pliocene folding phase. As the focus of this study is on the evolution of the surface structures in the Dehdasht Structural Basin and there is no clear data in depth to compare with the numerical models, the possible basement deformation is excluded in the experiments of this study. However, a controlling model considering the involvement of two basement faults is also conducted to confirm reliability of our initial setting for the reference model 1. Uplift of the hanging walls in the controlling model could be completely accommodated within the basal detachment in our reference model 1 and the resulted structures in the both models are comparable.

Furthermore, the surface processes applied in the simulations are based on a simplified diffusion law which do not account for complex erosion and sedimentation events dependent on erodibility, stream power-law fluvial systems, and so on, which are not always constant and may change through time and space.

5. Modelling results

In this section, the results of all the numerical experiments listed in Table 2 are presented. Each model was run for 1.5 Myr, which resulted in a total convergence of 15 km. Considering a total model width of 80 km, this corresponds to 19% of shortening, which is comparable to the shortening suggested to have taken place in the Dehdasht Basin (Section 2) and in most of the Dezful Embayment.

Each model developed two main anticlinal structures located above the velocity discontinuities imposed at the bottom boundary (Fig. 4). These two anticlines are rooted by left-verging thrust faults of the lower part of the lower competent layer.

5.1. Temporal evolution of the reference model 1

The temporal evolution of rock composition and the second invariant of the strain-rate tensor of the reference model 1 (see Table 2) are shown in Fig. 5. After 5 km shortening (0.5 Myr), two major box fold anticlines are formed above the velocity discontinuities separated by one open anticline of smaller amplitude (Fig. 5A). The major anticlines show a pop-up geometry since their two flanks are faulted by conjugate thrusts, as illustrated by the strain-rate plot (Fig. 5). Syntectonic processes provide sediments filling in the accommodation space away from the two major anticlines.

After 10 km of shortening (1 Myr), the foreland directed thrusts containing the larger tectonic displacement are the most active (Fig. 5B). These thrusts display a listric geometry rooting at the basal detachment and roofing at the upper competent layer (Fig. 5B). Decoupling along the intermediate detachment is observed by high strain-rates indicating fish-tail structures deforming the forelimbs of the two major anticlines (Fig. 5B). Syntectonic sedimentation is concentrated in the several minibasins subsiding into the thick upper detachment level.

After 15 km shortening (1.5 Myr), the thrusts in the lower competent layer further push the overlaying strata resulting in more asymmetric fold shapes of the upper competent layer (Fig. 5C). Fish-tail structures in front of the main SW-directed thrust cut through the upper component group reaching the surface as a reverse back-thrust. Furthermore, some branches of the intermediate detachment climb up to the surface through the crest of the large anticlines

(Fig. 5C). The growth of a minor fold/thrust zone in the central surficial basin, between the two large anticlines, affects distribution of its minibasins by forming two larger ones at the proximities and one smaller in the centre. Finally, after 20 km of shortening (2 Myr) the structures in both competent layers show a vergence towards the foreland with upright and overturned forelimbs (Fig. 5D). Subsiding minibasins above the upper weak detachment appear in form of growth synclines with a stratigraphic thickness of 2–3 km and a wavelength of ~5 km.

5.2. Role of syntectonic surface processes (model series 2 and 3)

First, experiments with equal coefficients for sedimentation and erosion are presented (model series 2). Then, the role of varying sedimentation diffusion coefficients with a fixed erosion coefficient (model series 3) is investigated. The competent layers show shorter-wavelength box folds with no vergence, in addition to the two main anticlines, when surface processes are absent (Fig. 6A; model 2a). The uppermost low-viscosity layer (upper detachment) becomes thinner (~800 m) above the growing anticlines and thicker (~2 km) within the coeval synclines (Fig. 6A). Applying syntectonic surface processes with a diffusion coefficient of 10^{-6} m^2/s results in an increase of ~1.5 km of the net displacement of the two main thrusts and the tightening of the anticlines (Fig. 6B; model 2b). Consequently, the smaller-scale box folds accommodate less shortening. Syntectonic sediments infill several minibasins of roughly 5 km width (Fig. 6B). The spatial distribution of these minibasins is controlled by the folding/faulting pattern of the competent layers. A surface diffusion coefficient of $2 \cdot 10^{-6}$ m^2/s shows similar characteristics of deformation and deposition as model 2b but with wider (0.5-1 km) and deeper (~200-300 m) minibasins and less pronounced box folds in between the major thrust faults (Fig. 6C; reference model 1). Further increase in surface diffusion ($\kappa = 5 \cdot 10^{-6}$ m^2/s) results in the lack of deformation between the two main anticlines and the growth of a large syncline infilling the space between them without extrusion of upper detachment material in between minibasins (Fig. 6D; model 2c). Finally, a very intense surface diffusion coefficient of 10^{-5} m^2/s involves larger but fewer minibasins with wavelengths of 10 km. More pronounced deformation and uplift of the two thrusts (about 800 m more than model 2c) is observed, with the intermediate detachment reaching to the surface locally (Fig. 6E; model 2d).

Models of series 3 exhibit a constant diffusion coefficient for erosion ($2\cdot10^{-6}$ m^2/s) while the intensity of sedimentation varies (Fig. 7; Table 2). In general, the impact of varying sedimentation on deformation of competent layers is similar as in model series 2. For experiments with relatively little sedimentation (reference model 1 and model 3a), an anticline develops within the competent layers in between the two main anticline-thrusts (Fig. 7). More intense sedimentation ($\kappa_{sed} = 5\cdot10^{-6}$-$10^{-5}$ m^2/s) diminishes the vertical growth of the two main conjugate fault systems (Fig. 7; models 3b and 3c). Furthermore, the intense sedimentation in models 3b and 3c leads to minibasins with larger wavelengths of about 8-10 km and increased stratigraphic thickness.

5.3. Influence of detachment thickness (model series 4 and 5)

Model series 4 shows experiments with varying thickness of the basal detachment (Fig. 8). When the basal detachment is relatively thin (T_b = 0.5 km), the larger fault-propagation folds of the upper competent layer above the main thrusts become roughly symmetric (Fig. 8A; model 4a). There, short wavelength folding (~13-20 km) occurs away from the main structures. Minibasins have short wavelengths (2–5 km) and are less abundant towards the centre of the model domain (Fig. 8A). Increasing thickness of the basal detachment (T_b = 1 km) leads to foreland-verging thrusted anticlines with close-to-vertical forelimbs and less dipping backlimbs (Fig. 8B; model 4b). Furthermore, minibasins become slightly wider (~1.5 km) and about 300 m deeper in contrast to the model with a 0.5 km thick basal detachment. In the experiment with a basal detachment of 1.5 km (Fig. 8C; reference model 1), a central anticline develops affecting syntectonic sedimentation and the distribution of related synclines in contrast to thinner basal detachment models.

Thickness variation of the upper detachment has considerable impact on both the syntectonic surface structures as well as on the subsurface geology (Fig. 9). An upper detachment thickness of 0.5 km leads to the formation of a central anticline between the two principal thrusted anticlines (Fig. 9A; model 5a). Minibasins show wavelengths depending on the underlying structures of the competent units. Thickening of the upper detachment results in more intense mechanical decoupling between the component group and the minibasins (Fig. 9B; reference model 1) and finally prevents deformation of the competent unit in the central part between principal anticlines (Fig 9C; model 5b). There, minibasins show little dependence of the underlying structures and steep side walls.

5.4. Influence of detachment viscosity (model series 6 and 7)

Model series 6 and 7 present the effect of viscosity variation of the different detachment levels (Figs. 10, 11). A relatively low viscosity of $\eta = 10^{18}$ Pa·s for the basal detachment results in thrusting and folding of the competent layers without any preferred vergence (Fig. 10A; model 6a). The developing folds and thrust sheets show wavelengths of 10 to 20 km and high amplitudes (Fig. 10A). Minibasins form within accommodation spaces resulting from the deformation of the competent unit. An increase of basal detachment viscosity to $5 \cdot 10^{18}$ Pa·s, results in leftward verging main thrust faults (Fig. 10B; model 6b). However, the growth of the minibasins does not change dramatically with respect to model 6a. Further increase of viscosity of the basal detachment reduces the amplitude of the central anticline but has little effect on the surface structures (Fig. 10C, D; reference model 1 and model 6c).

Viscosity of the upper detachment has a strong effect on the geometries of the minibasins and furthermore influences the deformation patterns of the competent unit (Fig. 11). A relatively low viscosity of the upper detachment ($\eta_u = 10^{18}$ Pa·s) leads to large sediment accumulation and vertical growth of minibasins that exhibit steep side walls (Fig. 11A; model 7a). Aside the two principal thrusted anticlines, the competent layers remain largely undeformed. A five- to ten-times increase in viscosity of the upper detachment, results in the development of a central anticline (Fig. 11B, C; model 7b and reference model 1). Minibasins grow slower and exhibit about two- to three-times larger wavelengths in contrast to the models with a very low upper detachment viscosity. A relatively strong upper detachment ($\eta_u = 10^{20}$ Pa·s) leads to wider (~9 km wide) and shallower dipping (~20°) growth synclines (Fig. 11D; model 7c). Little thickness variation of the upper detachment in the model 7c (Fig. 11D) indicates the absence of ductile flow and more coupling between the competent layers and the syntectonic sediments.

5.5. Style of syn-shortening minibasins

Syntectonic sedimentation leads to the subsidence of several minibasins into the uppermost detachment level along which they are ultimately decoupled from the competent layer. The volume of sedimentation in these minibasins is controlled mostly by the intensity of the surface processes and the strength of the upper detachment (Fig. 12). Increasing the surface processes increases the sediment volume in the minibasins (Fig. 12A). Decreasing the viscosity of the upper detachment level does not drastically change the volume of sedimentation except in model 7a. Very low viscosity of 10^{18} Pa· s for the upper detachment (model 7a) leads to a considerable increase in the sedimentation (Fig. 12B) comparable to the sediment volume of model 2d with intensive surface processes (Fig. 12A).

Vertical velocity (v_y) shows short-wavelength variation along surface structures bounded by the large anticlines while the underlying competent layer in this part show an almost uniform low velocity (Fig. 13). The lower v_y within and under the minibasins shows the subsidence between rising diapirs with increased vertical velocity. This velocity variation illustrates the distribution of minibasins and the shape of diapirs which have large wavelength in reference model 1 and model 5b (Fig. 13A and B) compared to model 7a with closely-spaced narrow diapirs and minibasins (Fig. 13C). Thicker salt source layer in model 5b ($T_u = 1.5$ km) leads to wider diapirs (Fig. 13B) compared to the reference model 1 with thinner and model 7a with lower viscous upper detachment (Fig. 13A and C).

Different types of minibasins are detectable from the experimental models of this study (Fig. 14). Dish-shape minibasins are the most common structures reproduced by the models although they may show different thicknesses and different wavelengths in models 2b, 6a and 7c (Fig. 14A, D and F). Bowl minibasins are also observed in models 3b, 6a and especially in model 7a (Fig. 14C, D, and E). Model 2d shows relatively flat-based minibasins containing upturned strata in form of halokinetic flaps along the walls of diapirs (Fig.14B).

6. Discussion

6.1. Syntectonic diapirism and sedimentation

Our experiments highlight how variations in compressional tectonics, diapirism and syntectonic sedimentation influence the style of surface structures (Section 5.5). To analyse the dynamic evolution of diapirs during convergence, vertical velocity of their rising top are plotted versus percent of shortening for different thickness and viscosity of the upper detachment layer (Fig. 15). Diapir rising velocities are fast at the beginning of the experiments (up to ~1 percent shortening; Fig. 15A, B), indicating that diapirs localize very rapidly. The same rising interval is detected in the vertical velocity of the minibasins (Fig. 15C, D), showing that no localized subsidence takes place initially. This stands in contrast to the evolution of diapirs rising slowly when the overburden is thin (Vendeville et al., 1993). After this initial step, the rise of diapirs decreases gently with increasing shortening and becomes constant after ~12% of shortening, except for model 7a. A sharp decrease in the vertical velocity of the minibasins after 2% of convergence (Fig. 15C, D) reveals they are not uplifting anymore and starting to subside (negative vertical velocity). Negative buoyancy of the minibasins causes evacuation of the salt from beneath of the subsiding minibasins toward the diapirs.

A thicker upper detachment level leads to faster diapir growth due to the larger volume of available incompetent material and consequently the lower viscous drag at the interface between the salt layer and the overburden (Fig. 15A; Vendeville et al., 1993). This observation agrees with numerical experiments by Fernandez and Kaus (2015), which show low potential of a diapir to rise from a thin salt layer with a thickness of 500 m compared to a 1.5 km salt layer for equal values of viscosity and sedimentation rate. Additionally, minibasins subside less into a thick incompetent layer (Fig. 15C); they start to have negative buoyancy earlier in the models with a thinner source layer than the models with a thicker one.

The lower the viscosity, the faster the upward motion of its diapirs (Chemia et al., 2008). However, in numerical experiments presented here, decreasing the viscosity of the upper incompetent layer has decreased the rise of diapirs especially in model 7a, except at the higher shortening of 16-19% where they show almost the same rate (Fig. 15B). Temporal v_y evolution of a diapir in model 7a from a very weak source layer (η_u = 10^{18} Pa· s) displays a considerable fluctuation; it shows an initial sharp rise followed by a considerable decrease in the diapir rising up to 6% shortening and another large increase interval from 6% to 19% of shortening (Fig. 15B, D). The minibasin formed in such a detachment level, gets negative buoyancy faster and more than those in the stronger incompetent layer (Fig. 15D), similar to the results of Fuchs et al. (2011) showing faster sinking of the sediments when salt viscosity decreases. The same decrease interval between 2 and 6% shortening is observed in the subsidence rate of the minibasin in model 7a (Fig. 15B). This is a result of the overburden thickening and the salt layer thinning due to fast sinking of the minibasin and consequent salt withdrawal, which increases the viscous drag within the salt layer (Vendeville et al., 1993). The salt flow increases again after 6% of shortening when the overburden subsidence is about 0.2 mm/yr (Fig. 15D). This may show that the subsidence of the minibasin has provided enough driving force to initiate the growth of its adjacent diapir as shown by Vendeville et al. (1993).

Calculated horizontal velocities within the upper detachment indicate gravity-induced flow from the growing anticlines towards the basin (Fig. 16). Viscous flow of the uppermost incompetent material toward the basin results in a significant thickening and accumulation of weak deposits in the centre of the basin affecting the dynamics of diapirism and minibasin growth (e.g., Dooley et al., 2017).

6.2 Comparison to the Dehdasht Structural Basin

The internal structure of the Dehdasht Basin is characterized by elongated synclines of variable wavelengths separated by ridges of Gachsaran evaporites with common SW-directed extrusions (Fig. 2). Synclinal depocenters containing growth wedges (e. g. Chengelva syncline, Fig. 2B) resemble asymmetric dish-shape minibasins (14A), typically developed in numerical experiments (models 2b, 4b, 5b and 7b). The geometry of the minibasins and that of the Gachsaran ridges can be compared to the results of numerical experiments in which appropriate material properties and surface process intensities can be specified. The relatively large area of Gachsaran outcrops and the relatively small thickness of the suprasalt deposits filling in the minibasins suggest a rather low depositional rate. Additionally, the ratio between regional accumulation rate of sediments above (after) the Gachsaran Formation (0.17 mm/yr; Oveisi et al., 2007) and the uplift rate of the MFF (1.2-2.5 mm/yr; Oveisi et al., 2009) in the Zagros fold belt is relatively low. To compare the effects of surface processes intensity obtained from numerical models to observation from the Dehdasht Basin, we used the non-dimensional surface diffusion coefficient ($\tilde{\kappa}$) proposed by Simpson (2006). If the ratio is below 1, the rate of surface processes is slow compared to the deformation rate. If $\tilde{\kappa} > 10$, surface processes become efficient in evolution of fold-thrust belt and piggyback basins (Simpson, 2006). Model 2b and the reference model 1 (Fig. 6) which have ratios smaller than 10 (Table 3) and therefore an almost low/intermediate rate of surface processes with respect to the deformation rate show the surface structures comparable to the Dehdasht Structural Basin.

The main structural effect of a thicker basal detachment, Hormuz salt, is the development of a medium amplitude anticline located between the two limiting larger amplitude anticlines, separating the two minibasins (Fig. 8C). The present low amplitude of this central anticline may indicate a relatively thin Hormuz salt underlying the Dehdasht Basin (Fig. 2B), in a similar way as proposed at larger scale by Bahroudi and Koyi (2003a). Furthermore, numerical models indicated that to initiate viscous flow, down building of minibasins, and diapiric rise and salt extrusion at least 1 km of original thickness of Gachsaran evaporites is needed (Fig. 9B, C). However, the strong decoupling between the Competent (subsalt) and Passive (suprasalt) groups across the Gachsaran evaporites (Fig. 2B) suggests an initial thickness of ductile evaporites of at least 1.5 km, similar to the model 5b (Fig. 9C). Comparing the structure of the subsalt Competent Group, the distribution of the Gachsaran evaporites, and the size and geometry of the minibasins from the Dehdasht Basin to the models, those with viscosities of $5\cdot10^{18}$ and 10^{19} Pa·s for the lower and upper detachments are the ones that approximate the natural example (Fig. 10 and 11). A viscosity of 10^{18} Pa·s for the lower detachment results in folding of the competent unit with shorter-wavelength ~14-17 km, which coincides with the results obtained by the Fars arc (Yamato et al., 2011) (Fig. 10A). A viscosity of 10^{18} Pa·s for the upper detachment generates very short-wavelength (2-3.5 km) and deep (2 km) minibasins that is not observed in the Dehdasht Basin (Figs. 11A and 2B). High upper detachment viscosities of 10^{20} Pa·s inhibits viscous flow and therefore distributes evenly the suprasalt deposition (Fig. 11D).

In summary, based on the modelling results, we propose a thickness of 0.5 km for the lower detachment and a minimum original thickness of 1.5 km for the Gachsaran upper detachment in the Dehdasht Basin. An average viscosities between $5 \cdot 10^{18}$ and 10^{19} Pa·s is proposed for both salt-bearing basal and upper detachment levels.. Accumulation rates were rather low compared to the deformation rate ($\tilde{\kappa} < 10$) to allow large scale extrusion of Gachsaran evaporites. Additionally, the development of asymmetric minibasins along the northern and southern boundaries of the Dehdasht basin is the consequence of the nature of the basal detachment and the structure of the Competent Group (Fig. 2B).

Using the results of the models that provide good estimations for the geological observables a sequential evolution is discussed (Fig. 17). The Dehdasht Structural Basin contains a multi-detachment stratigraphy that was shortened along a viscous basal detachment. The forelimbs of the high amplitude Khaviz and Kuh-e-Siah anticlines were faulted by foreland-directed thrusts rising from the basal detachment after 6% shortening (Fig. 17B). Between them, a smaller amplitude and symmetric Dehdasht anticline was formed. Syntectonic sediments, deposited above Gachsaran evaporites developed incipient minibasins. At around 12.5% of shortening, thicker growth synclines developed during the tightening of the major Khaviz and Kuh-e-Siah anticlines (Fig. 17C). After 19% convergence, the Khaviz and Kuh-e-Siah anticlines became narrower and higher above the propagating foreland-directed thrusts while the sedimentary load along the minibasins enhanced salt expulsion from below the synclines to the salt ridges (Figs 16-17D). The anomalously large thickness of the Gachsaran evaporites in the Dehdasht Basin is partially due to its gravitational flow from the rising Khaviz and Kuh-Siah anticlines toward the centre of basin as has been modelled at the scale of the entire fold and thrust belt by (Nilfouroushan et al., 2013) (Fig. 16).

7. Conclusions

We have run eighteen different 2D numerical experiments to better understand the tectono-sedimentary evolution of the Dehdasht Structural Basin in the SE Dezful Embayment in the Zagros Fold Belt. The results are as follows:

- Intermediate rate of sedimentation and erosion with respect to deformation rate (reference model 1; $\tilde{\kappa} < 10$) well approximate the natural example, including the growth of diapirs between relatively narrow growth synclines-minibasins during shortening.
- Well-developed diapirs within the Dehdasht Structural Basin form when the pre-shortening thickness of the Gachsaran evaporites (upper detachment) is greater than 1 km (Model 5b T_u = 1.5 km).
- Intermediate viscosity amounting between $5 \cdot 10^{18}$ and 10^{19} Pa·s for the upper detachment (Gachsaran evaporites) produce well-developed diapirs fitting observed ones. Higher viscosities (η_u=10^{20} Pa·s) do not develop diapirs whereas lower viscosity models (η_u=10^{18}) develop a large number of narrow, deep and highly asymmetric bowl minibasins.
- The present large calculated thickness of Gachsaran evaporites (2.5 km) filling the Dehdasht Basin is related to their gravity flow towards the basin from the growing limiting anticlines as observed by the horizontal velocity plots from models.
- Based on the model series 4, it is inferred that the potential 3 times thinner Hormuz salt layer beneath the Dehdasht Basin compared to its surrounding could have inhibited the

growth of detachment folds and thus developed a large structural depression surrounded by elevated anticlines.

- The growth history of the diapirs in the numerical experiments shows that shortening triggers the rapid initial growth of the diapirs when the sedimentation volume is not large enough to generate subsiding minibasins. Our models confirm that thickness and viscosity of the source salt layer are among the important parameters affecting the concomitant rising of diapirs separating sinking minibasin during compression.

Acknowledgements

This study is a part of the PhD dissertation of the corresponding author (KH) at Shahid Beheshti University that was partly developed during the scientific stay of KH in the ICTJA-CSIC of Barcelona. The authors would like to thank the Exploration Directorate of the N.I.O.C. for providing a part of the data used and to Jason Williams for the English improvements. We are grateful to Olivier Lacombe and Michel Faure for their comments that significantly improved the quality of the paper. JBR was supported by the Swiss National Science Foundation (Grant nr 2-77297-15). This research has been partially funded by projects Alpimed (PIE-CSIC-201530E082) and Subtetis (PIE-CSIC-201830E039).

References

Abdollahie Fard, I., Braathen, A., Mokhtari, M., Alavi, S.A., 2006. Interaction of the Zagros Fold-Thrust Belt and the Arabian-type, deep-seated folds in the Abadan Plain and the Dezful Embayment,SW Iran. Pet. Geosci. 12, 347–362. https://doi.org/10.1144/1354-079305-706

Abdollahie Fard, I., Sepehr, M., Serkati, S., 2011. Neogene salt in SW Iran and its interaction with Zagros folding. Geol. Mag. 148, 854–867. https://doi.org/10.1017/S0016756811000343

Agard, P., Omrani, J., Jolivet, L., Whitechurch, H., Vrielynck, B., Spakman, W., Monié, P., Meyer, B., Wortel, R., 2011. Zagros orogeny: A subduction-dominated process. Geol. Mag. 148, 692–725. https://doi.org/10.1017/S001675681100046X

Ahmadhadi, F., Lacombe, O., Daniel, JM., 2007. Early Reactivation of Basement Faults in Central Zagros (SW Iran): Evidence from Pre-folding Fracture Populations in Asmari Formation and Lower Tertiary Paleogeography. In: Lacombe, O., Roure, F., Lavé, J., Vergés, J. (eds) Thrust Belts and Foreland Basins. Frontiers in Earth Sciences. Springer, Berlin, Heidelberg.

https://doi.org/10.1007/978-3-540-69426-7_11

Alania, V.M., Chabukiani, A.O., Chagelishvili, R.L., Enukidze, O. V, 2015. Growth structures, piggy-back basins and growth strata of the Georgian part of the Kura foreland fold – thrust belt : implications for Late Alpine kinematic evolution. Geol. Soc. London, Spec. Publ. 428, 171–185.

Alavi, M., 2007. Structures of the Zagros fold-thrust belt in Iran. Am. J. Sci. 307, 1064–1095. https://doi.org/10.2475/09.2007.02

Bahroudi, A., Koyi, H., 2003a. Effect of spatial distribution of Hormuz salt on deformation style in the Zagros fold and thrust belt: an analogue modelling approach. J. Geol. Soc. London. 160, 719–733. https://doi.org/10.1144/0016-764902-135

Bahroudi, A., Koyi, H.A., 2004. Tectono-sedimentary framework of the Gachsaran Formation in the Zagros foreland basin. Mar. Pet. Geol. 21, 1295–1310. https://doi.org/10.1016/j.marpetgeo.2004.09.001

Bahroudi, A., Talbot, C.J., 2003b. The configuration of the basement beneath the Zagros Basin. J. Pet. Geol. 26, 257–282. https://doi.org/10.1111/j.1747-5457.2003.tb00030.x

Berberian, M., 1995. Master “blind” thrust faults hidden under the Zagros folds: active basement tectonics and surface morphotectonics. Tectonophysics 241, 193–224. https://doi.org/10.1016/0040-1951(94)00185-C

Bonini, M., 2003. Detachment folding, fold amplification, and diapirism in thrust wedge experiments. Tectonics 22. https://doi.org/10.1029/2002TC001458

Callot, J.-P., Trocmé, V., Letouzey, J., Albouy, E., Jahani, S., Sherkati, S., 2012. Pre-existing salt structures and the folding of the Zagros Mountains. Geol. Soc. London, Spec. Publ. 363, 545–561. https://doi.org/10.1144/SP363.27

Chanvry, E., Deschamps, R., Joseph, P., Puigdefàbregas, C., Poyatos-Moré, M., Serra-Kiel, J., Garcia, D., Teinturier, S., 2018. The influence of intrabasinal tectonics in the stratigraphic evolution of piggyback basin fills: Towards a model from the Tremp-Graus-Ainsa Basin (South-Pyrenean Zone, Spain). Sediment. Geol. 377, 34–62. https://doi.org/10.1016/J.SEDGEO.2018.09.007

Chemia, Z., Koyi, H., Schmeling, H., 2008. Numerical modelling of rise and fall of a dense layer in salt diapirs 798–816. https://doi.org/10.1111/j.1365-246X.2007.03661.x

Crameri, F., Schmeling, H., Golabek, G.J., Duretz, T., Orendt, R., Buiter, S.J.H., May, D.A., Kaus, B.J.P., Gerya, T. V, Tackley, P.J., 2012. geodynamic modelling : an evaluation of the “ sticky air ” method. Geophys. J. Int. 189, 38–54. https://doi.org/10.1111/j.1365-246X.2012.05388.x

Decelles, P.G., Giles, K.A., 1996. Foreland basin systems. Basin Res. 8, 105–123.

Demercian, S., Szatmari, P., Cobbold, P.R., 1993. Style and pattern of salt diapirs due to thin-skinned gravitational gliding, Campos and Santos basins, offshore Brazil. Tectonophysics 228, 393–433. https://doi.org/10.1016/0040-1951(93)90351-J

Derikvand, B., Alavi, S.A., Fard, I.A., Hajialibeigi, H., 2018. Folding style of the Dezful Embayment of Zagros Belt: Signatures of detachment horizons, deep-rooted faulting and syn-deformation deposition. Mar. Pet. Geol. 91, 501–518. https://doi.org/10.1016/j.marpetgeo.2018.01.030

Dooley, T.P., Hudec, M.R., Carruthers, D., Jackson, M.P.A., Luo, G., 2017. The effects of base-salt relief on salt flow and suprasalt deformation patterns — Part 1 : Flow across simple steps in the base of salt. INterpretations 5, 1–23.

Edgell, H.S., 1996. Salt tectonism in the Persian Gulf Basin. Geol. Soc. London, Spec. Publ. 100, 129–151. https://doi.org/10.1144/GSL.SP.1996.100.01.10

Ehrenberg, S.N., Pickard, N.A.H., Laursen, G. V, Monibi, S., Mossadegh, Z.K., Svånå, T.A., Aqrawi, A.A.M., McArthur, J.M., Thirlwall, M.F., 2007. Strontium isotope stratigraphy of the asmari formation (Oligocene - Lower miocene), SW Iran. J. Pet. Geol. 30, 107–128. https://doi.org/10.1111/j.1747-5457.2007.00107.x

Fernandez, N., Kaus, B.J.., 2015. Pattern formation in 3-D numericalmodels of down-built diapirs initiated by a Rayleigh–Taylor instability. Geophys. J. Int. 202, 1253–1270. https://doi.org/10.1093/gji/ggv219

Fort, X., Brun, J.P., Chauvel, F., 2004. Salt tectonics on the Angolan margin, synsedimentary deformation processes. Am. Assoc. Pet. Geol. Bull. 88, 1523–1544. https://doi.org/10.1306/06010403012

Harrison, J.C., Jackson, M.P.A., 2014. Exposed evaporite diapirs and minibasins above a canopy in central Sverdrup Basin, Axel Heiberg Island, Arctic Canada. Basin Res. 26, 567–596. https://doi.org/10.1111/bre.12037

Hessami, K., Koyi, H.A., Talbot, C.J., Tabasi, H., Shabanian, E., 2001. Progressive unconformities within an evolving foreland fold – thrust belt , Zagros Mountains. J. Geol. Soc. London 158, 969–981.

Homke, S., Vergés, J., Garcés, M., Emami, H., Karpuz, R., 2004. Magnetostratigraphy of Miocene-Pliocene Zagros foreland deposits in the front of the Push-e Kush Arc (Lurestan Province, Iran). Earth Planet. Sci. Lett. 225, 397–410. https://doi.org/10.1016/j.epsl.2004.07.002

Hudec, M.R., Jackson, M.P.A., Schultz-ela, D.D., 2009. The paradox of minibasin subsidence into salt : Clues to the evolution of crustal basins. GSA Bull. 121, 201–221. https://doi.org/10.1130/B26275.1

Jackson, M.P.A., Hudec, M.R., 2017. Salt tectonics : principles and practice. Cambridge University Press. https://doi.org/https://doi.org/10.1017/9781139003988

Jahani, S., Callot, J., Letouzey, J., Lamotte, D.F. De, 2009. The eastern termination of the Zagros Fold-and-Thrust Belt, Iran : Structures, evolution, and relationships between salt plugs, folding, and faulting, Tectonics 28, 1–22. https://doi.org/10.1029/2008TC002418

Kergaravat, C., Ribes, C., Callot, J.P., Ringenbach, J.C., 2017. Tectono-stratigraphic evolution of salt-controlled minibasins in a fold and thrust belt, the Oligo-Miocene central Sivas Basin. J. Struct. Geol. 102, 75–97. https://doi.org/10.1016/j.jsg.2017.07.007

Kergaravat, C., Ribes, C., Legeay, E., Callot, J.P., Kavak, K.S., Ringenbach, J.C., 2016. Minibasins and salt canopy in foreland fold-and-thrust belts: The central Sivas Basin, Turkey. Tectonics 35, 1342–1366. https://doi.org/10.1002/2016TC004186

Khadivi, S., Mouthereau, F., Larrasoana, J. C., Verges, J., Lacombe, O., Khademi, E., Beamud, E., Melinte-Dobrinescu, M., and Suc, J. P., 2010. Magnetochronology of synorogenic Miocene foreland sediments in the Fars arc of the Zagros Folded Belt (SW Iran), Basin Res., 22(6), 918–932.

Lacombe, O., Bellahsen, N., 2016. Thick-skinned tectonics and basement-involved fold–thrust belts: insights from selected Cenozoic orogens. Geol. Mag., 1-48, doi:10.1017/S0016756816000078

Lees, G.M., 1952. Foreland folding. Q. J. Geol. Soc. 108, 1–34. https://doi.org/10.1144/GSL.JGS.1952.108.01-04.02

Legeay, E., Ringenbach, J.-C., Kergaravat, C., Pichat, A., Mohn, G., Vergés, J., Kavak, K.S., Callot, J.-P., 2019. Structure and kinematics of the Central Sivas Basin (Turkey): Salt deposition and tectonics in an evolving fold-and-thrust belt. Geol. Soc. London, Spec. Publ. 490, SP490-

2019-92. https://doi.org/10.1144/SP490-2019-92

Llewellyn, P. G., 1973. Dehdasht geological compilation map, 1:100000. National Iranian Oil Company.

Martori, G.L., Taril, G.C., Lehmann, C.T., 2000. Evolution of the angolan passive margin, West Africa, with emphasis on post-salt structural styles. Geophys. Monogr. Ser. 115, 129–149. https://doi.org/10.1029/GM115p0129

Mouthereau, F., Lacombe, O., Vergés, J., 2012. Building the Zagros collisional orogen: Timing, strain distribution and the dynamics of Arabia/Eurasia plate convergence. Tectonophysics. https://doi.org/10.1016/j.tecto.2012.01.022

Mcleod, J. H., and Akbari Y., 1970. Behbahan geological compilation map, 1:100000. National Iranian Oil Company.

Mukherjee, S., Talbot, C.J., Koyi, H.A., 2010. Viscosity estimates of salt in the Hormuz and Namakdan salt diapirs, Persian Gulf. Geol. Mag. 147, 497–507. https://doi.org/10.1017/S001675680999077X

Najafi, M., Vergés, J., Etemad-Saeed, N., Karimnejad, H.R., 2018. Folding, thrusting and diapirism: Competing mechanisms for shaping the structure of the north Dezful Embayment, Zagros, Iran. Basin Res. 30, 1200–1229. https://doi.org/10.1111/bre.12300

Najafi, M., Yassaghi, A., Bahroudi, A., Vergés, J., Sherkati, S., 2014. Impact of the Late Triassic Dashtak intermediate detachment horizon on anticline geometry in the Central Frontal Fars, SE Zagros fold belt, Iran. Mar. Pet. Geol. 54, 23–36. https://doi.org/10.1016/j.marpetgeo.2014.02.010

Narimani, H., Yassaghi, A., Hassan Goudarzi, M.G., 2012. Structural Analysis of Dowgonbadan Region, Zagros Fold Thrust Belt, An Instance of Frontal and Lateral Ramp. Geol. Soc. Iran, Geosci. 21, 53–64 (in Persian).

Navabpour, P., Barrier, E., Mcquillan, H., 2014. Oblique oceanic opening and passive margin irregularity, as inherited in the Zagros fold-and-thrust belt. Terra Nov. 26, 208–215. https://doi.org/10.1111/ter.12088

Nilfouroushan, F., Pysklywec, R., Cruden, A., Koyi, H., 2013. Thermal-mechanical modeling of salt-based mountain belts with pre-existing basement faults: Application to the Zagros fold and thrust belt, southwest Iran. Tectonics 32, 1212–1226. https://doi.org/10.1002/tect.20075

O'Brien, C. A. E., 1950. Tectonic problems of the oil field belt of southwest Iran. Proceedings of 18th International Geological Congress, London: Part 6, p. 45–58.

O'Brien, C.A.E., 1957. Salt Diapirism in south Persia. Geologie en Mijnbouw. Geol. en Mijnb. 19, 357–376.

Ori, G.G., Friend, P.F., 1984. Sedimentary basins formed and carried piggyback on active thrust sheets. Geology 12, 475–478. https://doi.org/10.1130/0091-7613(1984)12<475

Oveisi, B., Lavé, J., and Van der Beek, P., 2007. Active foldinganddeformationrate at the centralZagros front (Iran), in Thrust Belts and Foreland Basins: From Fold Kinematics to Hydrocarbon Systems, edited by O. Lacombe et al., pp. 267-287, Springer, New York.

Oveisi, B., Lavé, J., van der Beek, P., Carcaillet, J., Benedetti, L., Aubourg, Ch., 2009. Thick- and thin-skinned deformation rates in the central Zagros simple folded zone (Iran) indicated by displacement of geomorphic surfaces. Geophys. J. Int. 176, 627–654. https://doi.org/10.1111/j.1365-246X.2008.04002.x

Pirouz, M., Simpson, G., Chiaradia, M., 2015. Constraint on foreland basin migration in the Zagros mountain belt using Sr isotope stratigraphy. https://doi.org/10.1111/bre.12097

Ringenbach, J., Salel, J., Kergaravat, C., Ribes, C., Bonnel, C., Callot, J.-P., 2013. Salt tectonics in the Sivas Basin, Turkey: outstanding seismic analogues from outcrops. First Break 31, 57–65.

Rowan, M.G., Lawton, T.F., Giles, K.A., Ratliff, R.A., 2003. Near-salt deformation in La Popa basin, Mexico, and the northern Gulf of Mexico: A general model for passive diapirism. Am. Assoc. Pet. Geol. Bull. 87, 733–756. https://doi.org/10.1306/01150302012

Ruh, J.B., 2017. Effect of fluid pressure distribution on the structural evolution of accretionary wedges. Terra Nov. 29, 202–210. https://doi.org/10.1111/ter.12263

Ruh, J.B., Hirt, A.M., Burg, J., Mohammadi, A., 2014. Forward propagation of the Zagros Simply Folded Belt constrained from magnetostratigraphy of growth strata. Tectonics 33, 1534–1551. https://doi.org/10.1002/2013TC003465.

Ruh, J.B., Vergés, J., 2018. Effects of reactivated extensional basement faults on structural evolution of fold-and-thrust belts: Insights from numerical modelling applied to the Kopet Dagh Mountains. Tectonophysics 746, 493–511. https://doi.org/10.1016/j.tecto.2017.05.020

Sattarzadeh, Y., Cosgrove, J.W., Vita-Finzi, C., 2002. The geometry of structures in the Zagros cover rocks and its neotectonic implications. Geol. Soc. London, Spec. Publ. 195, 205–217. https://doi.org/https://doi.org/10.1144/GSL.SP.2002.195.01.11

Sepehr, M., Cosgrove, J., Moieni, M., 2006. The impact of cover rock rheology on the style of folding in the Zagros fold-thrust belt. Tectonophysics 427, 265–281. https://doi.org/10.1016/j.tecto.2006.05.021

Sepehr, M., Cosgrove, J.W., 2007. The role of major fault zones in controlling the geometry and spatial organization of structures in the Zagros Fold-Thrust Belt. Geol. Soc. London, Spec. Publ. 272, 419–436. https://doi.org/10.1144/GSL.SP.2007.272.01.21

Sepehr, M., Cosgrove, J.W., 2004. Structural framework of the Zagros Fold-Thrust Belt, Iran. Mar. Pet. Geol. 21, 829–843. https://doi.org/10.1016/j.marpetgeo.2003.07.006

Sherkati, S., Letouzey, J., 2004. Variation of structural style and basin evolution in the central Zagros (Izeh zone and Dezful Embayment), Iran. Mar. Pet. Geol. 21, 535–554. https://doi.org/10.1016/j.marpetgeo.2004.01.007

Sherkati, S., Letouzey, J., De Lamotte, D.F., 2006. Central Zagros fold-thrust belt (Iran): New insights from seismic data, field observation, and sandbox modeling. Tectonics 25, 1–27. https://doi.org/10.1029/2004TC001766

Sherkati, S., Molinaro, M., Frizon de Lamotte, D., Letouzey, J., 2005. Detachment folding in the Central and Eastern Zagros fold-belt (Iran): Salt mobility, multiple detachments and late basement control. J. Struct. Geol. 27, 1680–1696. https://doi.org/10.1016/j.jsg.2005.05.010

Simpson, GDH., 2006. Modelling interactions between fold–thrust belt deformation, foreland flexure and surface mass transport. Basin Research 18, 125–143.

Talling, J., Lawton, F., Burbank, W., Hobbs, S., 1995. Evolution of latest Cretaceous – Eocene nonmarine deposystems in the Axhandle piggyback basin of central Utah. GSA Bull. 107, 297–315.

Vendeville, B. C., and Jackson, M. P. A., 1993, Rates of extension and deposition determine whether growth faults or salt diapirs form, in : Armentrout, J. M., Bloch, Roger, Olson, H. C., and Perkins, B. F., eds., Rates of Geologic Processes, Society of Economic Paleontologists and Mineralogists, Gulf Coast Section, 14th Annual Research Conference Program and Extended Abstracts, p. 263-268.

Vendeville, B.C., Nilsen, K.T., 1995. Episodic Growth of Salt Diapirs Driven by Horizontal Shortening. Adapt. from Ext. Abstr. Prep. conjunction with oral Present. 16th Annu. Res. Conf. January, 1995 285–295.

Vergés, J., Emami, H., Garcés, M., Beamud, E., Homke, S., Skott, P., 2019. Zagros Foreland Fold Belt Timing Across Lurestan to Constrain Arabia–Iran Collision. Dev. Struct. Geol. Tectonics 3, 29–52. https://doi.org/10.1016/B978-0-12-815048-1.00003-2

Vergés, J., Goodarzi, M.G.H., Emami, H., 2011a. Multiple Detachment Folding in Pusht-e Kuh Arc, Zagros: Role of Mechanical Stratigraphy. AAPG Mem. 94, 69–94. https://doi.org/10.1306/13251333M942899

Vergés, J., Saura, E., Casciello, E., Fernandez, M., Villaseñor, A., Jiménez-Munt, I., García-Castellanos, D., 2011b. Crustal-scale cross-sections across the NW Zagros belt : implications for the Arabian margin reconstruction. Geol. Mag. 148, 739–761. https://doi.org/10.1017/S0016756811000331

Volozh, Y., Talbot, C., Ismail-Zadeh, A., 2003. Salt structures and hydrocarbons in the Pricaspian basin. Am. Assoc. Pet. Geol. Bull. 87, 313–334. https://doi.org/10.1306/09060200896

Worrall, D., M., Sneslson, S., 1989. Evolution of the northern Gulf of Mexico with emphasis on Cenozoic growth faulting and the role of salt, in: Bally, A., W., Palmer, A.R. (Eds.), The Goology of North America: An Overview. Geological Society of America, pp. 97–138.

Yamato, P., Kaus, B.J.P., Mouthereau, F., Castelltort, S., 2011. Dynamic constraints on the crustal-scale rheology of the Zagros fold belt, Iran 815–818. https://doi.org/10.1130/G32136.1

Figure captions

Fig. 1. A) Tectono-stratigraphic subdivisions of the Zagros fold-and-thrust belt (based on Sherkati and Letouzey, 2004 and Vergés et al., 2011a). UDMA: Urumieh-Dokhtar Magmatic Arc; MZF: Main Zagros Fault; HZF: High Zagros Fault; MFF: Mountain Front Fault; M-ZTF: Minab-Zendan Transfer Fault; BRF: Balarud Fault; KzF: Kazerun Fault, Kj: Kamaraj segment; SF: Surmeh Fault; HBF: Hendijan-Bahregansar Fault (or paleo-high); KMF: Kharg-Mish Fault (or paleo-high); IFZ: Izeh Fault Zone; nDZ: north Dezful; sDZ: south Dezful. B) Topographic map of the Dehdasht Structural Basin, south Dezful Embayment.

Fig. 2. A) Geological map of the study area (after Llewellyn, 1973 and McLeod & Akbari, 1970). The deposits located out of the study area are transparent. B) Cross section across the study area showing the Dehdasht Basin as a large syncline containing several smaller synclines filled by Mishan, Aghajari and Bakhtyari formations, decoupled from the Competent Group by the thick Gachsaran evaporites. The cross-section from the Lower Cretaceous down to the basement (dashed lines) is based on the stratigraphy available for the Dezful Embayment (e. g. Alavi, 2007 and Sherkati et al., 2006) and the present topography map of the Zagros basement (Motiei, 1993). Location of the section is indicated in (A).

Fig. 3. Stratigraphic column of the study area based on geological maps (after Llewellyn, 1973 and McLeod & Akbari, 1970), well data from the Khaviz anticline (NIOC, unpublished report), and Alavi (2007) and Sherkati et al. (2006). Mechanical behaviour is based on O'Brien (1950). Absolute ages are based on strontium isotope dating: Ages of base and top of Asmari Formation from Khaviz anticline (Ehrenberg et al., 2007); ages for Mishan Formation from Aghajari anticline to the southeast (Pirouz et al., 2015). Thickness of Gachsaran Formation is calculated by the restoration of the regional cross-sections across the Dehdasht using area constant method.

Fig. 4. Model setup. Initial geometry includes 8 km of stratigraphic sequence and 7 km of sticky-air. Two velocity discontinuities are located at the lower boundary (black dots) localizing deformation during compression.

Fig. 5. Temporal evolution of the reference model 1. Left column: Rock composition. Right column: Second invariant of the strain-rate tensor. 1, 2: fore- and back-thrust; 3: connection of the basal detachment to the intermediate one (fish-tail structure); 4: steeper frontal limb compared to the previous step; 5: branches of intermediate detachment reaching to the surface; 6: upright frontal limb. Black dots in the strain rate plots show the location of the velocity discontinuities.

Fig. 6. Model series 2 shows experiments with varying surface diffusion coefficients (for both sedimentation and erosion) after 15 km of convergence. A) Model 2a without surface processes. B) Model 2b, $\kappa = 10^{-6}$ m^2/s. C) Reference model 1, $\kappa = 2\cdot10^{-6}$ m^2/s. D) Model 2c, $\kappa = 5\cdot10^{-6}$ m^2/s. E) Model 2d, $\kappa = 10^{-5}$ m^2/s. Increasing surface processes increases wavelengths of minibasins and prohibits formation of a central low-amplitude anticline in between the two

main thrusts/folds in the competent layers. The colours dark greyish red, light lime and light grey display basal, intermediate and upper detachments, respectively. Light green colour shows the competent layer, and syntectonic deposits are shown by alternative black and yellow. The light blue colour on the right of the models is related to incoming material.

Fig. 7. Model series 3 shows experiments with different sedimentation values after 15 km of convergence. Erosion is considered constant with a diffusion coefficient of $2\cdot10^{-6}$ m^2/s. A) Model 3a, $\kappa_{sed} = 10^{-6}$ m^2/s. B) Reference model 1, $\kappa_{sed} = 2\cdot10^{-6}$ m^2/s. C) Model 3b, $\kappa_{sed} = 5\cdot10^{-6}$ m^2/s D) Model 3c, $\kappa_{sed} = 10^{-5}$ m^2/s. Higher sediment diffusion coefficient increases wavelength and stratigraphic thickness of the minibasins and also diminishes formation of conjugate fault systems in the competent layers. Colour code as for Fig. 6.

Fig. 8. Model series 4 shows experiments with varying thickness of the basal detachment after 15 km of convergence. A) Model 4a, T_b = 500 m. B) Model 4b, T_b = 1 km. C) Reference model 1, T_b = 1.5 km. In these models diffusion coefficients for the both sedimentation and erosion are equal. Decreasing thickness of the basal detachment prevents formation of a high-amplitude anticline in between the two large anticlines and decreases the wavelength of minibasins. Colour code as for Fig. 6.

Fig. 9. Model series 5 shows experiments with varying of thickness of the upper detachment after 15 km of convergence. A) Model 5a, T_u = 500 m. B) Reference model 1, T_u = 1 km. C) Model 5b, T_u = 1.5 km. In these models diffusion coefficients for the both sedimentation and erosion are equal. Increasing thickness of the upper detachment decreases wavelengths of the minibasins and causes well-developed diapirs. It also prevents formation of a central anticline between the two large anticlines. Colour code as for Fig. 6.

Fig. 10. Model series 6 shows experiments with varying viscosity (η) for the basal detachment after 15 km of convergence. A) Model 6a, $\eta_b = 10^{18}$ Pa·s. B) Model 6b, $\eta_b = 5\cdot10^{18}$ Pa·s. C) Reference model 1, $\eta_b = 10^{19}$ Pa·s. D) Model 6c, $\eta_b = 10^{20}$ Pa·s. In these models diffusion coefficients for the both sedimentation and erosion are equal. Decreasing viscosity of the basal detachment increases the role of competent layers' structures on distribution of minibasins. Colour code as for Fig. 6.

Fig. 11. Model series 7 shows experiments with varying viscosity for the upper detachment after 15 km of convergence. A) Model 7a, $\eta_u = 10^{18}$ Pa·s. B) Model 7b, $\eta_u = 5\cdot10^{18}$ Pa·s. C) Reference model 1, $\eta_u = 10^{19}$ Pa·s. D) Model 7c, $\eta_u = 10^{20}$ Pa·s. In these models diffusion coefficients for the both sedimentation and erosion are equal. Decreasing viscosity of the upper detachment forms short-wavelength deep minibasins while increasing its viscosity increases wavelengths and sizes of the minibasins and also amplitude of the central anticline between the two large anticlines. Colour code as for Fig. 6.

Fig. 12. Temporal evolution of the sedimentation volume per kilometre after 15 km shortening. A) Model series 2 (surface processes intensity) and B) model series 7 (upper detachment

viscosity) compared to the reference model. Increasing the intensity of surface processes increases sediment volume. Very low viscous upper detachment (model 7a) causes accumulation of syntectonic sedimentation comparable to that provided by high surface processes in model 2d.

Fig. 13. Vertical velocity graphs (v_y) for surface structures. A) Reference model 1. B) Model 5b, T_u = 1.5 km. C) Model 7a, $\eta_u = 10^{18}$ Pa·s. Rising diapirs have higher velocity compared to the subsiding minibasins. Vertical velocities mimic distribution of minibasins and shape of diapirs.

Fig. 14. Line drawing for different types of minibasins developed in numerical experiments. A) Asymmetric dish-shape minibasin, typical minibasins over the basal slope (model 2b). B) Elongated flat-based minibasin showing halokinetic flaps along walls of diapirs (model 2d). C) Bowl minibasins with shrinkage to the surface and halokinetic flaps along the narrow cylinder and flare diapirs (model 3b). D) Bowl and symmetric dish-shape minibasins controlled by structural style of competent layers (model 6a). E) Very deep, narrow minibasin and narrow flare and taper diapirs (model 7a). F) Elongated dish-shape minibasin almost parallel to the underlying competent layer (model 7c). Thin blue lines show surface topography of minibasins and red lines highlight the shape of diapirs.

Fig. 15. Role of thickness and viscosity of the uppermost detachment level on the vertical velocity (v_y) of the diapirs and minibasins. A and C) v_y temporal history for diapirs and minibasins in a salt layer with different thickness. A thicker upper detachment level leads to faster diapir growth and less minibasin subsidence. B and D) v_y temporal history for diapirs and minibasins in a salt layer with different viscosity. Decreasing the viscosity of the upper incompetent layer (η_u) decreases the rising of diapirs except at the higher shortening where they show almost the same rate. While a very low viscous salt layer results in a faster subsiding minibasin. The v_y profile has been plotted for vertical velocity of the top of first diapirs and base of the second minibasins, from the right side, located between the two large anticlines.

Fig. 16. Two-dimensional horizontal velocity (model 5b) illustrating thickening of the upper detachment due to salt flow. A) After 6% of shortening, and B) after 19% shortening.

Fig. 17. Proposed evolution of the Dehdasht Structural Basin with 1.5 km upper detachment (Miocene Gachsaran evaporites), 1.5 km basal detachment (Cambrian Hormuz Salt) and moderate syntectonic surface processes ($\kappa = 2 \cdot 10^{-6}$). It proposes that the large Khaviz and Kuh-e-Siah anticlines of the Dehdasht Basin are developed from symmetric box folds over conjugate faults to fault-propagation folds after 19% shortening. It also suggests the well development of diapirism and minibasins in the Dehdasht Basin after ~12% shortening. Numbers 1 to 3 correspond to the Kuh-e-Siah, deep-root of the Dehdasht and the Khaviz anticlines, respectively. The black lines show the thrust faults formed in the competent layers during convergence. Colour code as for Fig. 6.

Fig. 1

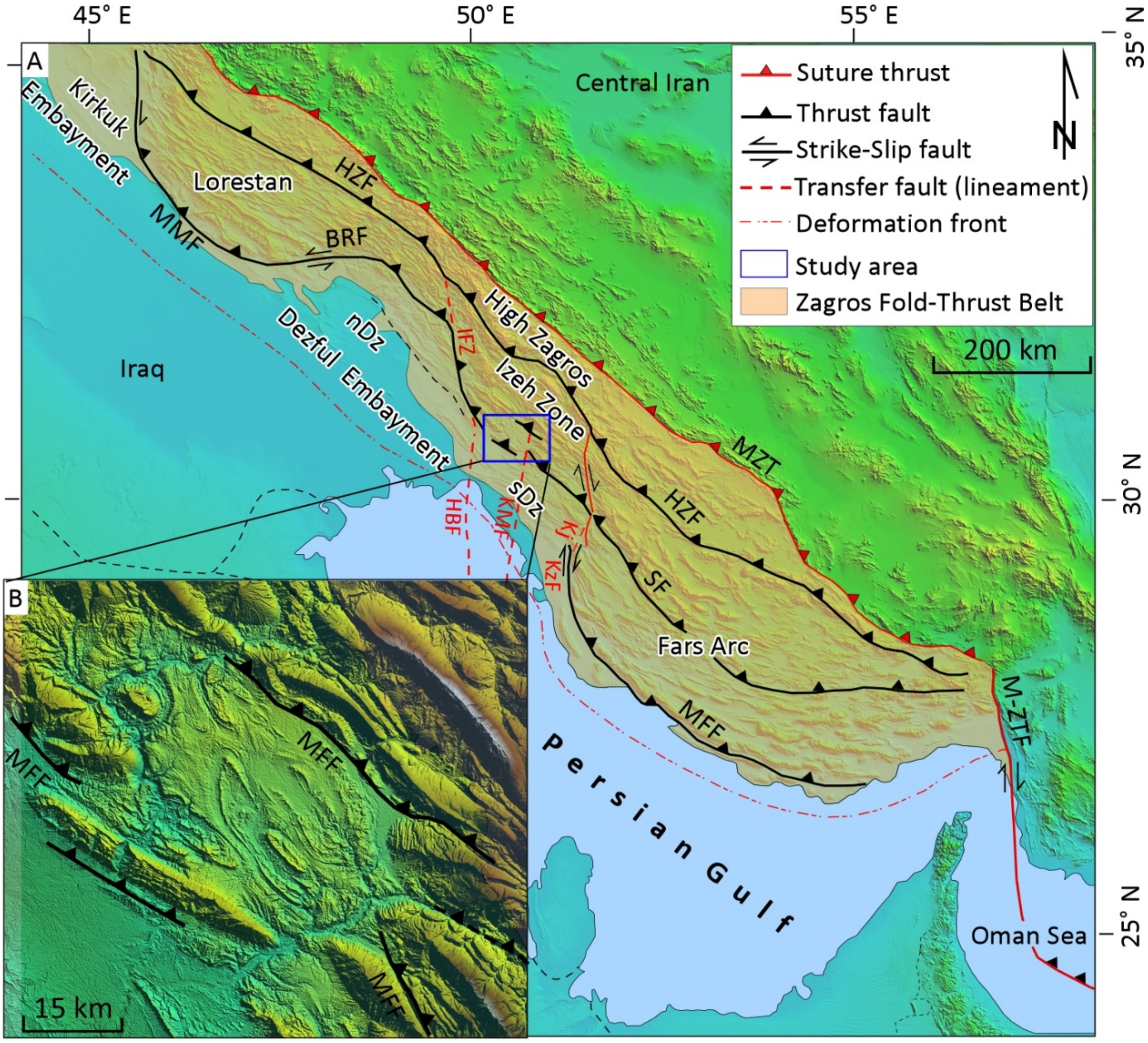
45° E
50° E
55° E
35° N
30° N
25° N
A
Suture thrust
Thrust fault
Strike-Slip fault
Transfer fault (lineament)
Deformation front
Study area
Zagros Fold-Thrust Belt
N
200 km
Central Iran
Kirkuk Embayment
Lorestan
HZF
MMF
BRF
nDz
IFZ
High Zagros
Iraq
Dezful Embayment
Izeh Zone
MZT
sDz
HBF
KMF
KzF
HZF
SF
Fars Arc
MFF
M-ZTF
Persian Gulf
Oman Sea
B
MFF
MFF
MFF
15 km

Fig. 2

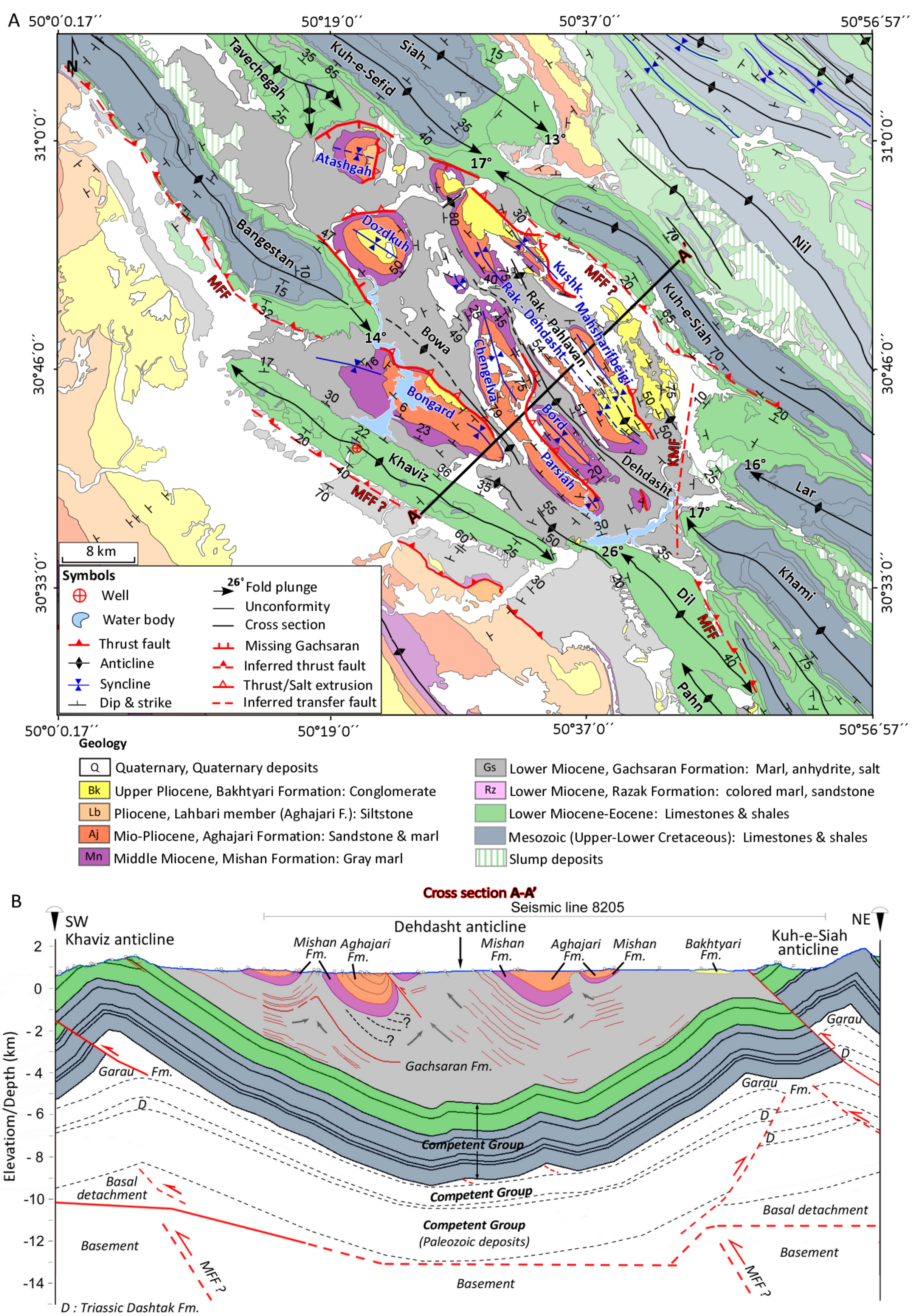
A
50°0´0.17´´
50°19´0´´
50°37´0´´
50°56´57´´
31°0´0´´
30°46´0´´
30°33´0´´
N
Tavechegah
Kuh-e-Sefid
Siah
Atashgah
Dozdkuh
Bangestan
MFF
MFF ?
Kushk - Mahsharifbeigi
Rak - Dehdasht
Rak - Pahlavan
Chengelva
Bowa
Bongard
Bord
Parsian
Dehdasht
Khaviz
KMF
Kuh-e-Siah
Nil
Lar
Khami
Dil
Pahn
8 km
Symbols
Well
Water body
Thrust fault
Anticline
Syncline
Dip & strike
Fold plunge
Unconformity
Cross section
Missing Gachsaran
Inferred thrust fault
Thrust/Salt extrusion
Inferred transfer fault
Geology
Q Quaternary, Quaternary deposits
Bk Upper Pliocene, Bakhtyari Formation: Conglomerate
Lb Pliocene, Lahbari member (Aghajari F.): Siltstone
Aj Mio-Pliocene, Aghajari Formation: Sandstone & marl
Mn Middle Miocene, Mishan Formation: Gray marl
Gs Lower Miocene, Gachsaran Formation: Marl, anhydrite, salt
Rz Lower Miocene, Razak Formation: colored marl, sandstone
Lower Miocene-Eocene: Limestones & shales
Mesozoic (Upper-Lower Cretaceous): Limestones & shales
Slump deposits
B
Cross section A-A'
Seismic line 8205
SW
Khaviz anticline
Dehdasht anticline
NE
Kuh-e-Siah anticline
Mishan Fm.
Aghajari Fm.
Bakhtyari Fm.
Gachsaran Fm.
Garau Fm.
Competent Group
Competent Group (Paleozoic deposits)
Basal detachment
Basement
MFF ?
Elevatiom/Depth (km)
D : Triassic Dashtak Fm.

Fig. 3

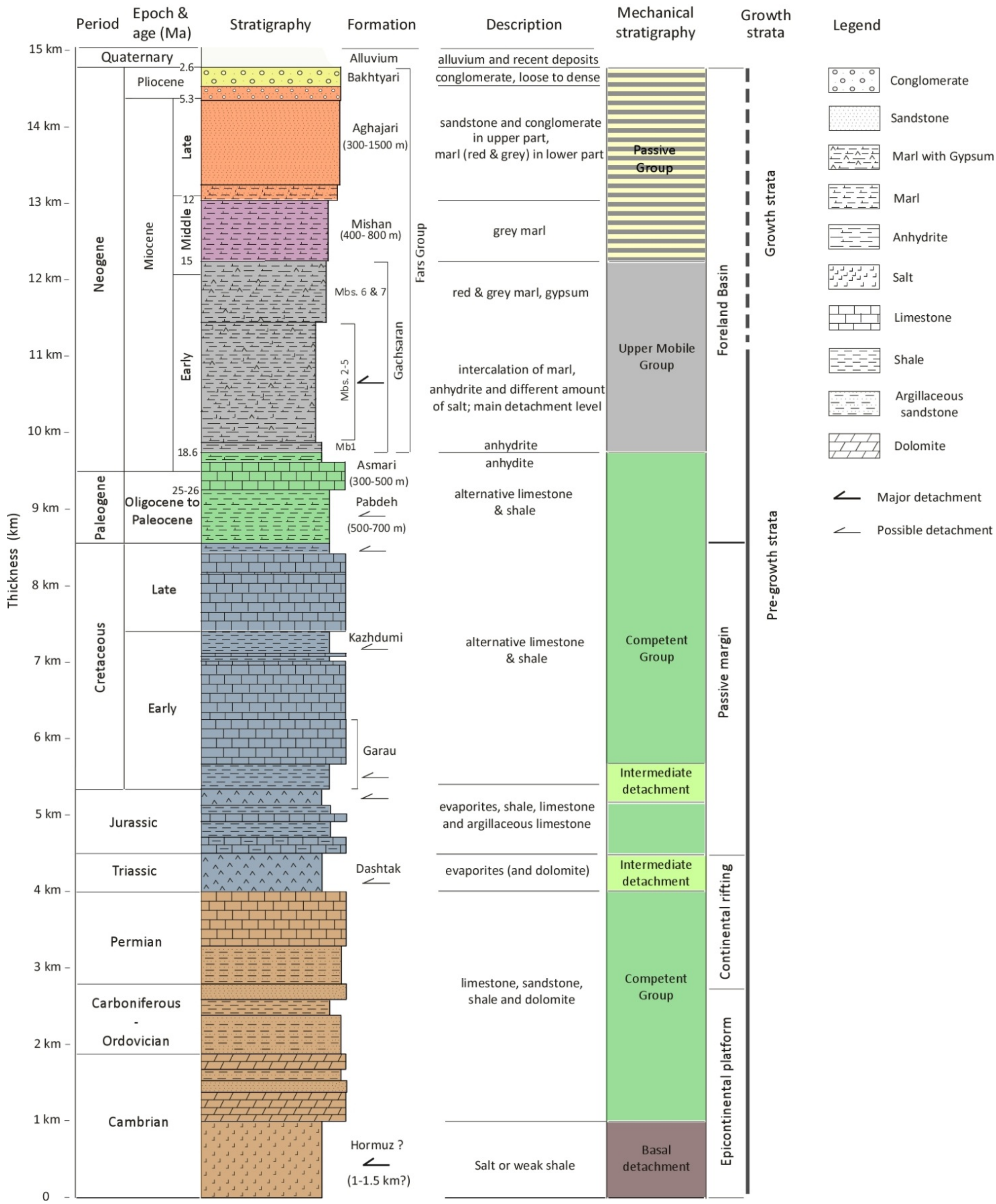

Period
Epoch & age (Ma)
Stratigraphy
Formation
Description
Mechanical stratigraphy
Growth strata
Legend
Thickness (km)
15 km
14 km
13 km
12 km
11 km
10 km
9 km
8 km
7 km
6 km
5 km
4 km
3 km
2 km
1 km
0
Quaternary
Neogene
Pliocene
Miocene
Late
Middle
Early
2.6
5.3
12
15
18.6
Paleogene
Oligocene to Paleocene
25-26
Cretaceous
Late
Early
Jurassic
Triassic
Permian
Carboniferous - Ordovician
Cambrian
Alluvium
Bakhtyari
Aghajari (300-1500 m)
Mishan (400- 800 m)
Fars Group
Mbs. 6 & 7
Mbs. 2-5
Gachsaran
Mb1
Asmari (300-500 m)
Pabdeh (500-700 m)
Kazhdumi
Garau
Dashtak
Hormuz ? (1-1.5 km?)
alluvium and recent deposits
conglomerate, loose to dense
sandstone and conglomerate in upper part, marl (red & grey) in lower part
grey marl
red & grey marl, gypsum
intercalation of marl, anhydrite and different amount of salt; main detachment level
anhydrite
anhydite
alternative limestone & shale
alternative limestone & shale
evaporites, shale, limestone and argillaceous limestone
evaporites (and dolomite)
limestone, sandstone, shale and dolomite
Salt or weak shale
Passive Group
Upper Mobile Group
Competent Group
Intermediate detachment
Intermediate detachment
Competent Group
Basal detachment
Foreland Basin
Passive margin
Continental rifting
Epicontinental platform
Growth strata
Pre-growth strata
Conglomerate
Sandstone
Marl with Gypsum
Marl
Anhydrite
Salt
Limestone
Shale
Argillaceous sandstone
Dolomite
Major detachment
Possible detachment

Fig. 4

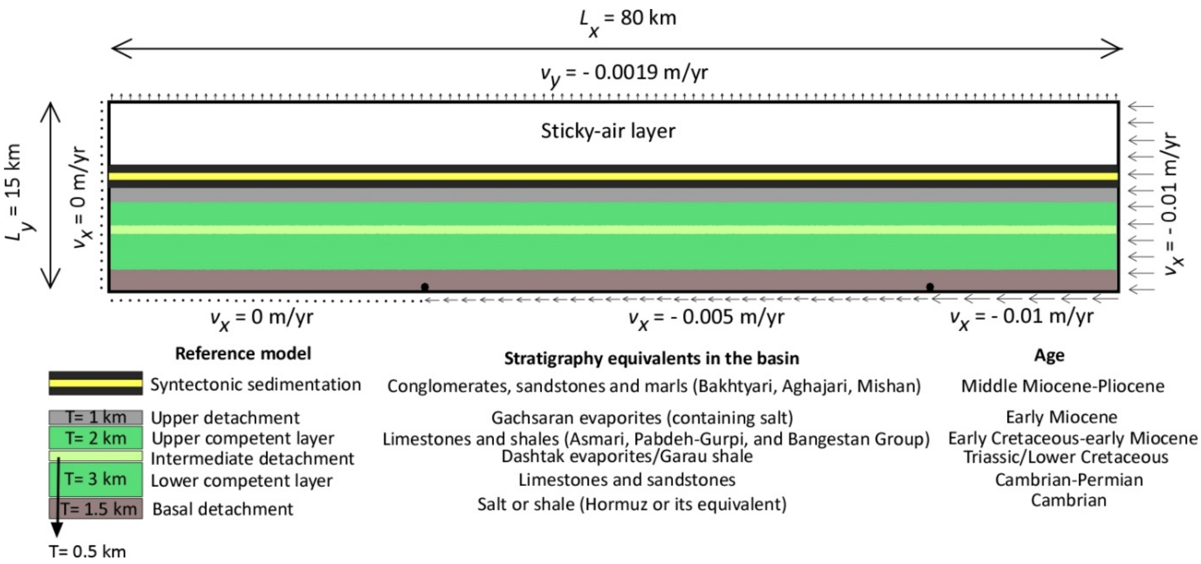

L_x = 80 km
v_y = - 0.0019 m/yr
Sticky-air layer
L_y = 15 km
v_x = 0 m/yr
v_x = - 0.01 m/yr
v_x = 0 m/yr
v_x = - 0.005 m/yr
v_x = - 0.01 m/yr
Reference model
Stratigraphy equivalents in the basin
Age
Syntectonic sedimentation
Conglomerates, sandstones and marls (Bakhtyari, Aghajari, Mishan)
Middle Miocene-Pliocene
T= 1 km
Upper detachment
Gachsaran evaporites (containing salt)
Early Miocene
T= 2 km
Upper competent layer
Limestones and shales (Asmari, Pabdeh-Gurpi, and Bangestan Group)
Early Cretaceous-early Miocene
Intermediate detachment
Dashtak evaporites/Garau shale
Triassic/Lower Cretaceous
T= 3 km
Lower competent layer
Limestones and sandstones
Cambrian-Permian
T= 1.5 km
Basal detachment
Salt or shale (Hormuz or its equivalent)
Cambrian
T= 0.5 km

Fig. 5

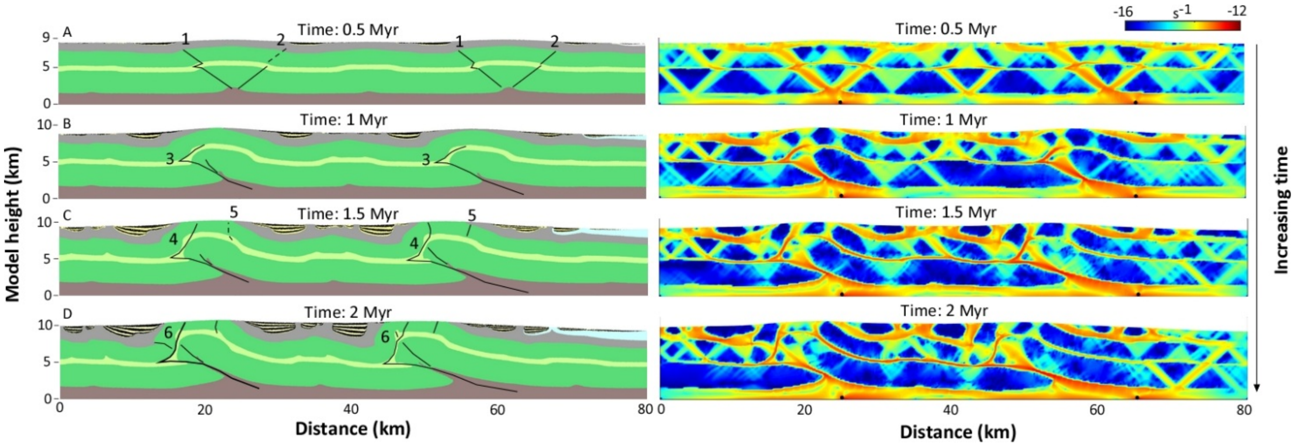
A
Time: 0.5 Myr
B
Time: 1 Myr
C
Time: 1.5 Myr
D
Time: 2 Myr
Model height (km)
Distance (km)
-16
s^{-1}
-12
Increasing time

Fig. 6

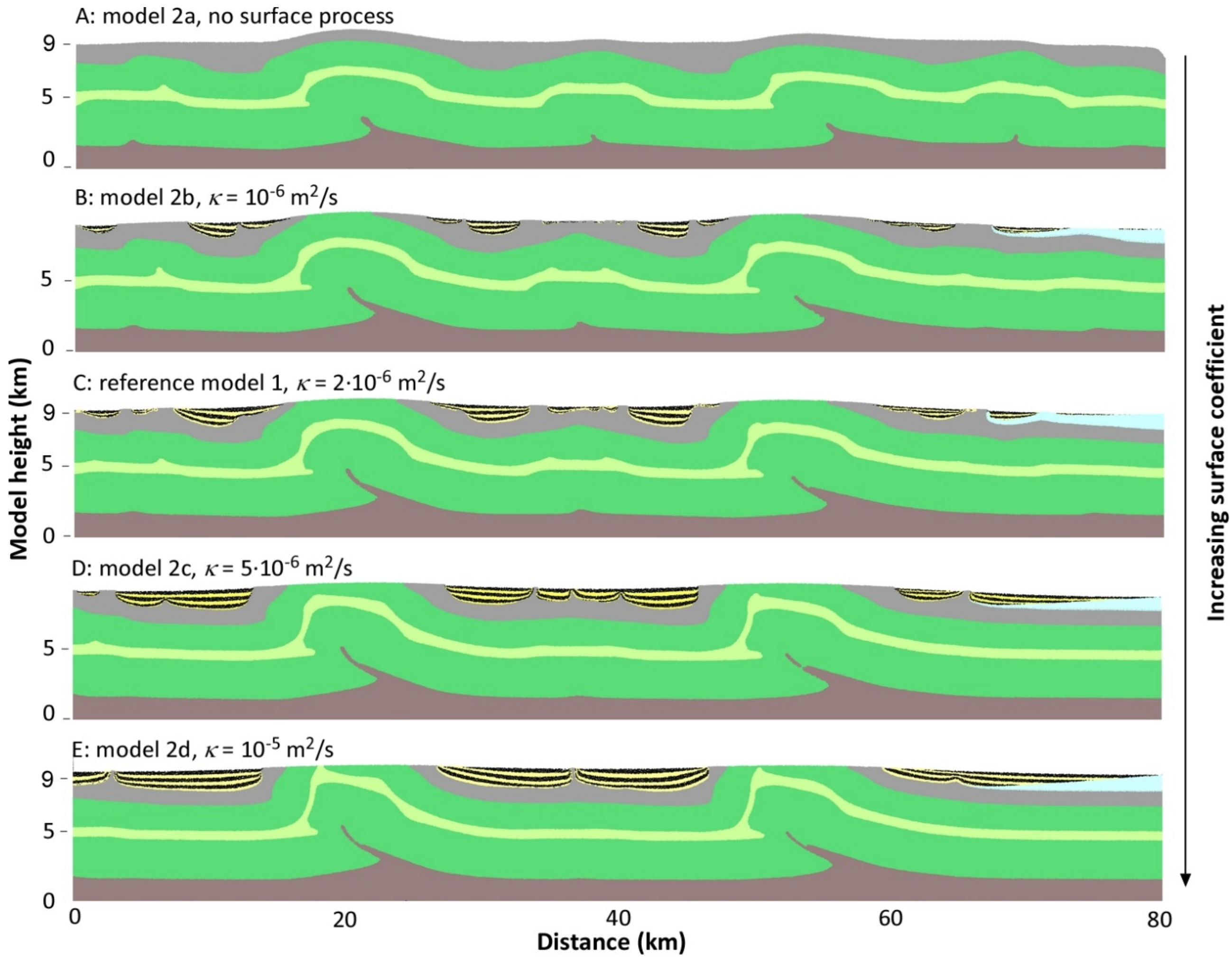
A: model 2a, no surface process
B: model 2b, $\kappa = 10^{-6}$ m^2/s
C: reference model 1, $\kappa = 2\cdot10^{-6}$ m^2/s
D: model 2c, $\kappa = 5\cdot10^{-6}$ m^2/s
E: model 2d, $\kappa = 10^{-5}$ m^2/s
Model height (km)
9
5
0
0
20
40
60
80
Distance (km)
Increasing surface coefficient

Fig. 7

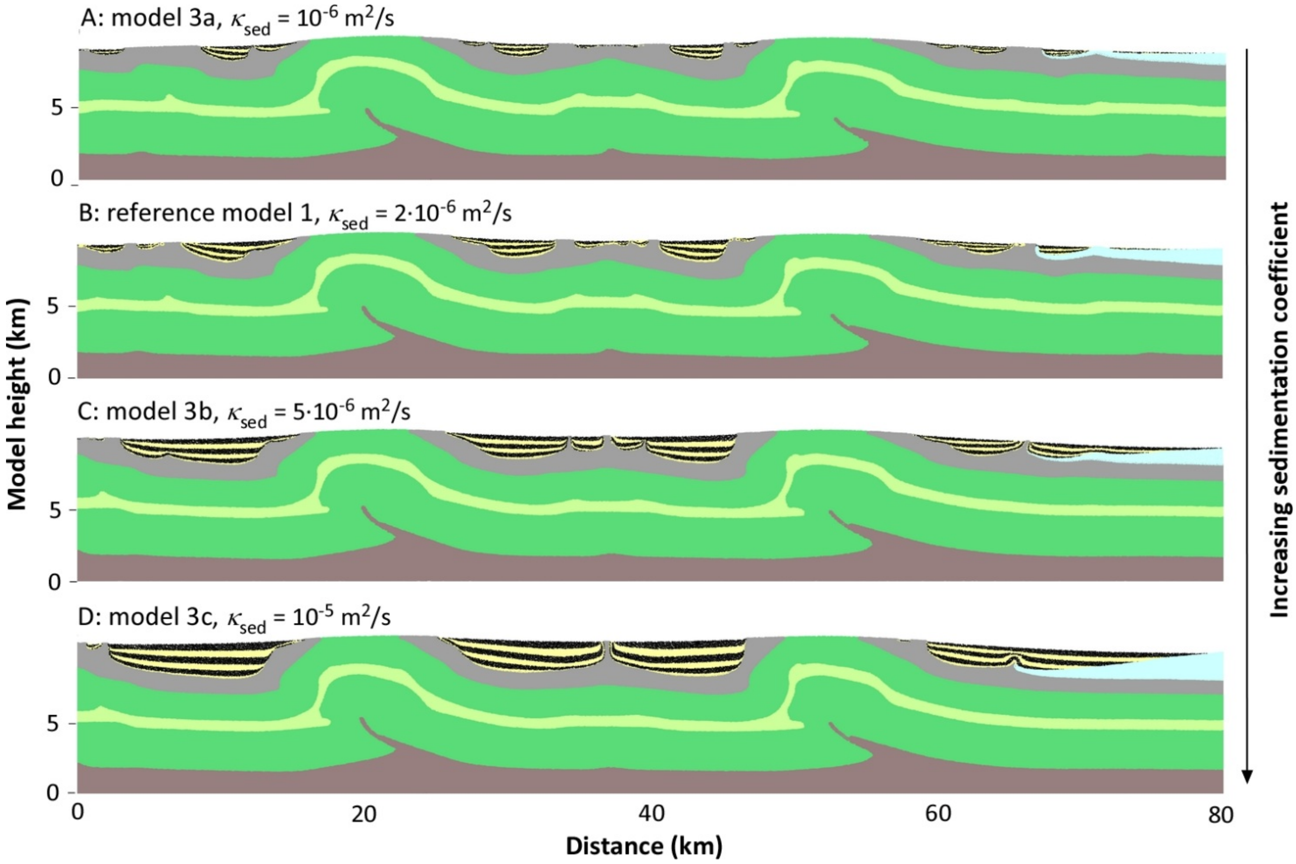
A: model 3a, κ_{sed} = 10^{-6} m^2/s
B: reference model 1, κ_{sed} = $2\cdot10^{-6}$ m^2/s
C: model 3b, κ_{sed} = $5\cdot10^{-6}$ m^2/s
D: model 3c, κ_{sed} = 10^{-5} m^2/s
Model height (km)
Distance (km)
Increasing sedimentation coefficient
0
5
0
20
40
60
80

Fig. 8

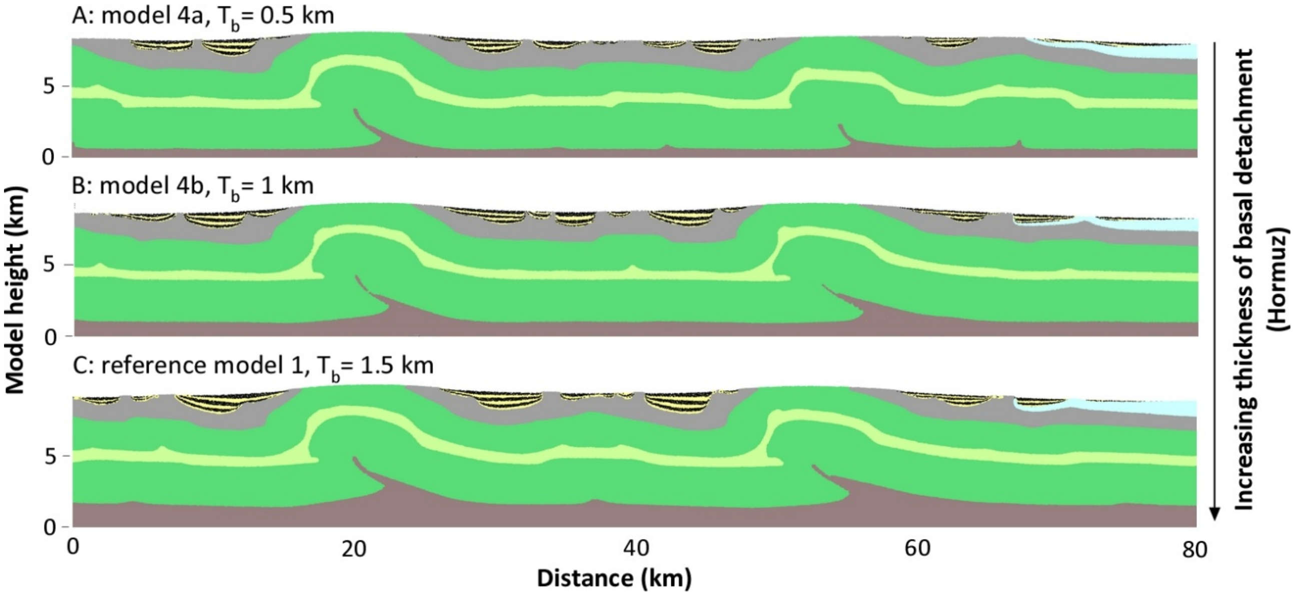
A: model 4a, T_b= 0.5 km
B: model 4b, T_b= 1 km
C: reference model 1, T_b= 1.5 km
Model height (km)
Distance (km)
0
5
0
20
40
60
80
Increasing thickness of basal detachment (Hormuz)

Fig. 9

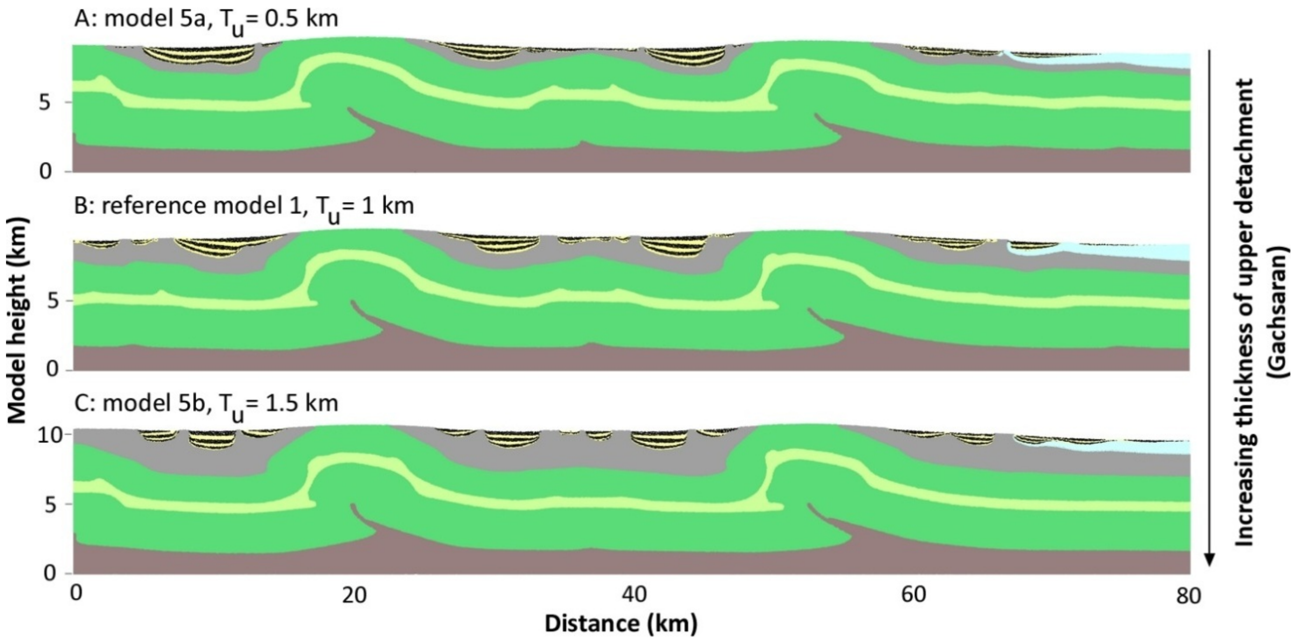

A: model 5a, T
u
= 0.5 km
B: reference model 1, T
u
= 1 km
C: model 5b, T
u
= 1.5 km
Model height (km)
0
5
10
0
20
40
60
80
Distance (km)
Increasing thickness of upper detachment
(Gachsaran)

Fig. 10

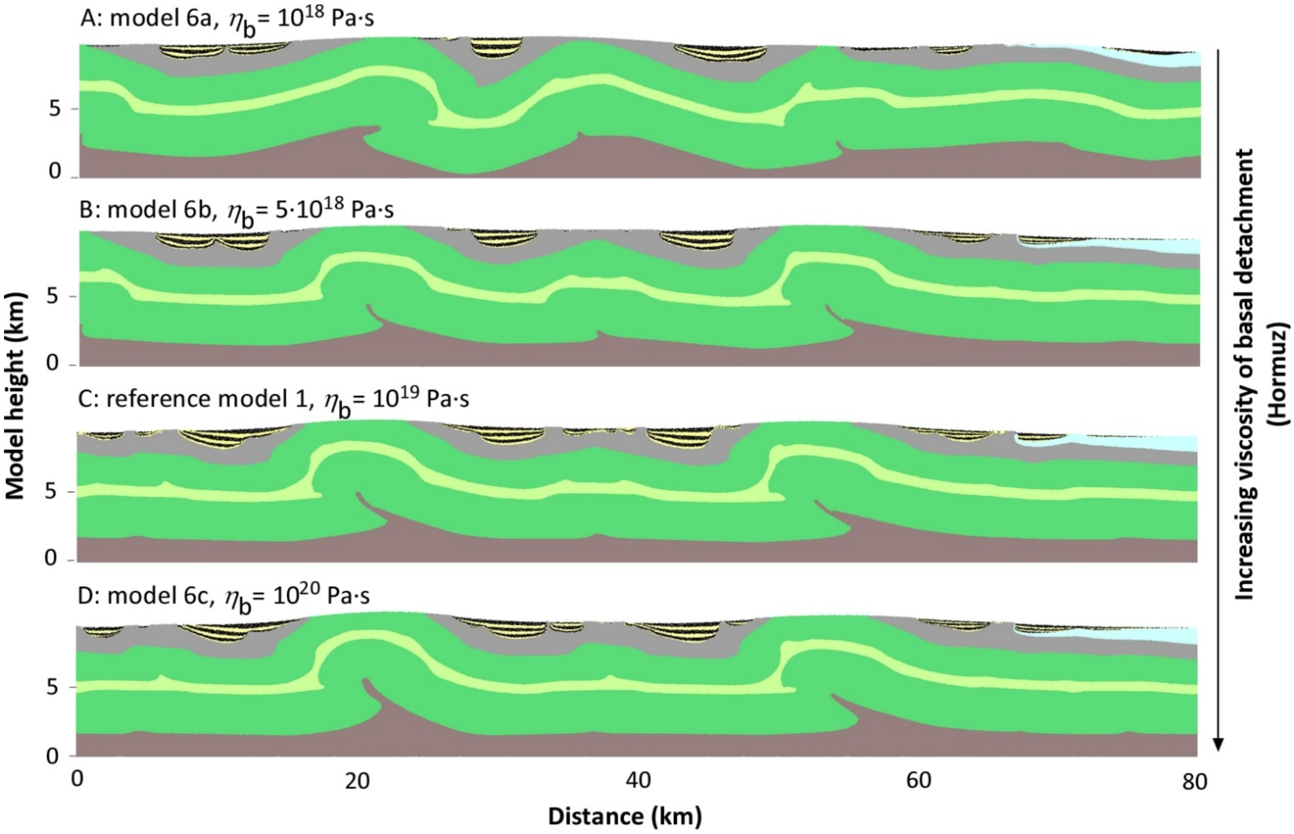

A: model 6a, η_b= 10^{18} Pa·s
B: model 6b, η_b= $5{\cdot}10^{18}$ Pa·s
C: reference model 1, η_b= 10^{19} Pa·s
D: model 6c, η_b= 10^{20} Pa·s
Model height (km)
0
5
0
20
40
60
80
Distance (km)
Increasing viscosity of basal detachment (Hormuz)

Fig. 11

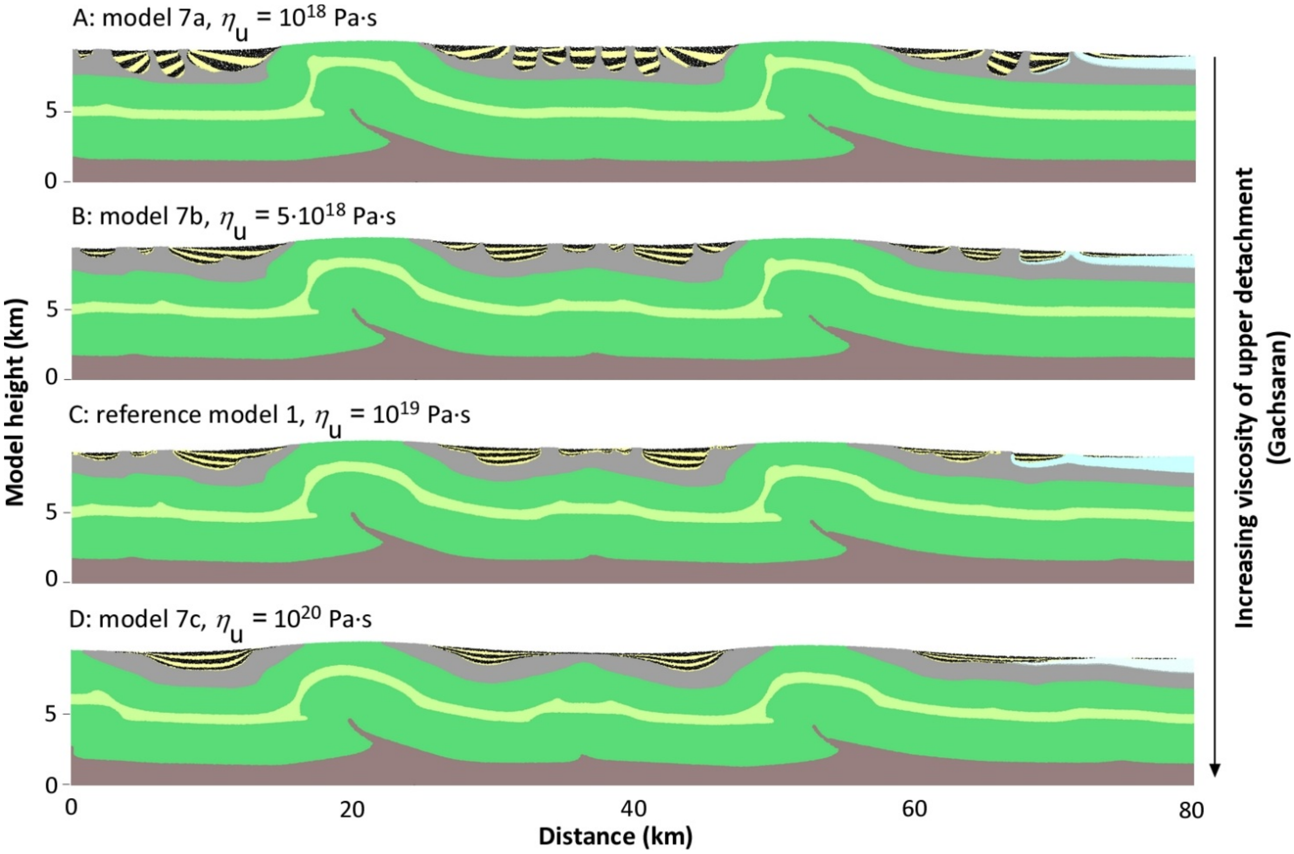

A: model 7a, η_u = 10^{18} Pa·s
B: model 7b, η_u = $5 \cdot 10^{18}$ Pa·s
C: reference model 1, η_u = 10^{19} Pa·s
D: model 7c, η_u = 10^{20} Pa·s
Model height (km)
0
5
Distance (km)
0
20
40
60
80
Increasing viscosity of upper detachment (Gachsaran)

Fig. 12

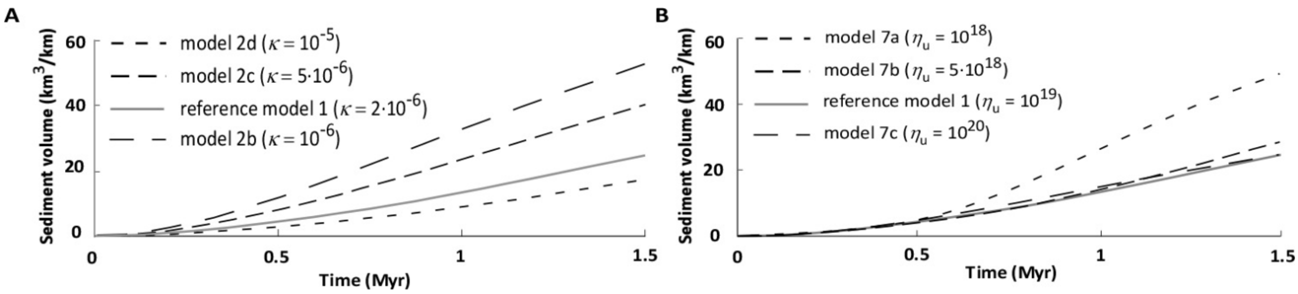
A
model 2d ($\kappa = 10^{-5}$)
model 2c ($\kappa = 5 \cdot 10^{-6}$)
reference model 1 ($\kappa = 2 \cdot 10^{-6}$)
model 2b ($\kappa = 10^{-6}$)
Sediment volume (km^3/km)
Time (Myr)
0
20
40
60
0.5
1
1.5
B
model 7a ($\eta_u = 10^{18}$)
model 7b ($\eta_u = 5 \cdot 10^{18}$)
reference model 1 ($\eta_u = 10^{19}$)
model 7c ($\eta_u = 10^{20}$)
Sediment volume (km^3/km)
Time (Myr)

Fig. 13

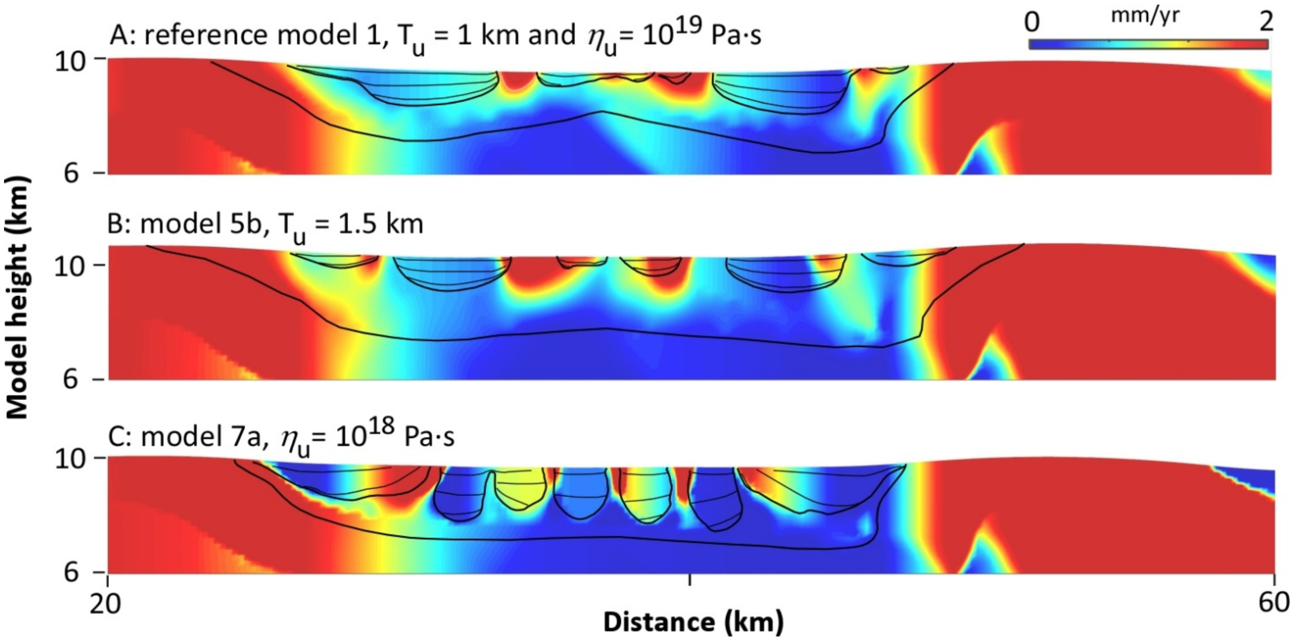

A: reference model 1, T_u = 1 km and η_u= 10^{19} Pa·s
0
mm/yr
2
10
6
Model height (km)
B: model 5b, T_u = 1.5 km
10
6
C: model 7a, η_u= 10^{18} Pa·s
10
6
20
60
Distance (km)

Fig. 14

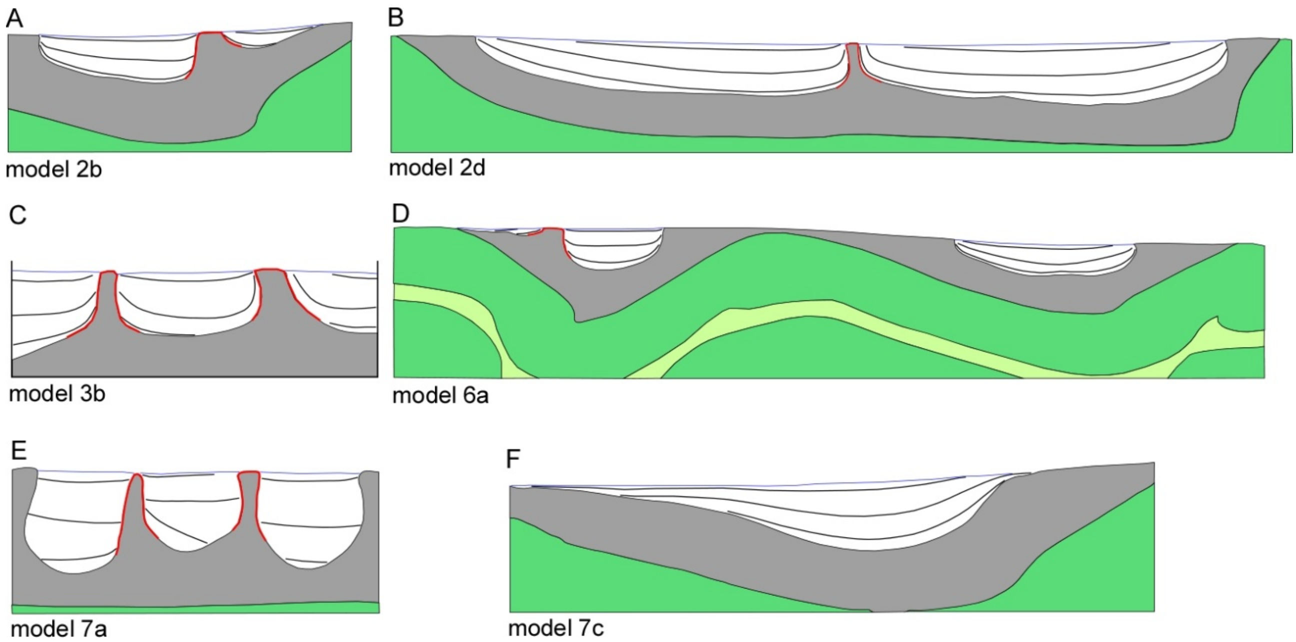

Fig. 15

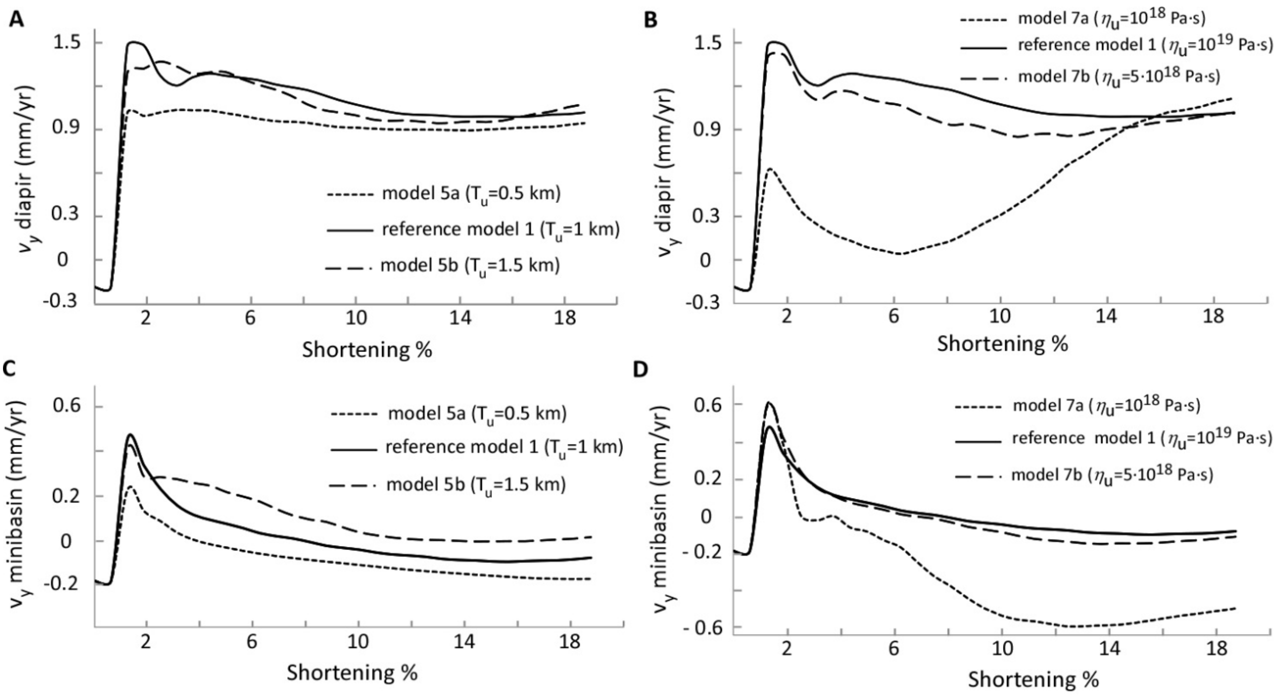
A
v_y diapir (mm/yr)
Shortening %
model 5a (T_u=0.5 km)
reference model 1 (T_u=1 km)
model 5b (T_u=1.5 km)
B
v_y diapir (mm/yr)
Shortening %
model 7a (η_u=10^{18} Pa·s)
reference model 1 (η_u=10^{19} Pa·s)
model 7b (η_u=5·10^{18} Pa·s)
C
v_y minibasin (mm/yr)
Shortening %
model 5a (T_u=0.5 km)
reference model 1 (T_u=1 km)
model 5b (T_u=1.5 km)
D
v_y minibasin (mm/yr)
Shortening %
model 7a (η_u=10^{18} Pa·s)
reference model 1 (η_u=10^{19} Pa·s)
model 7b (η_u=5·10^{18} Pa·s)

Fig. 16

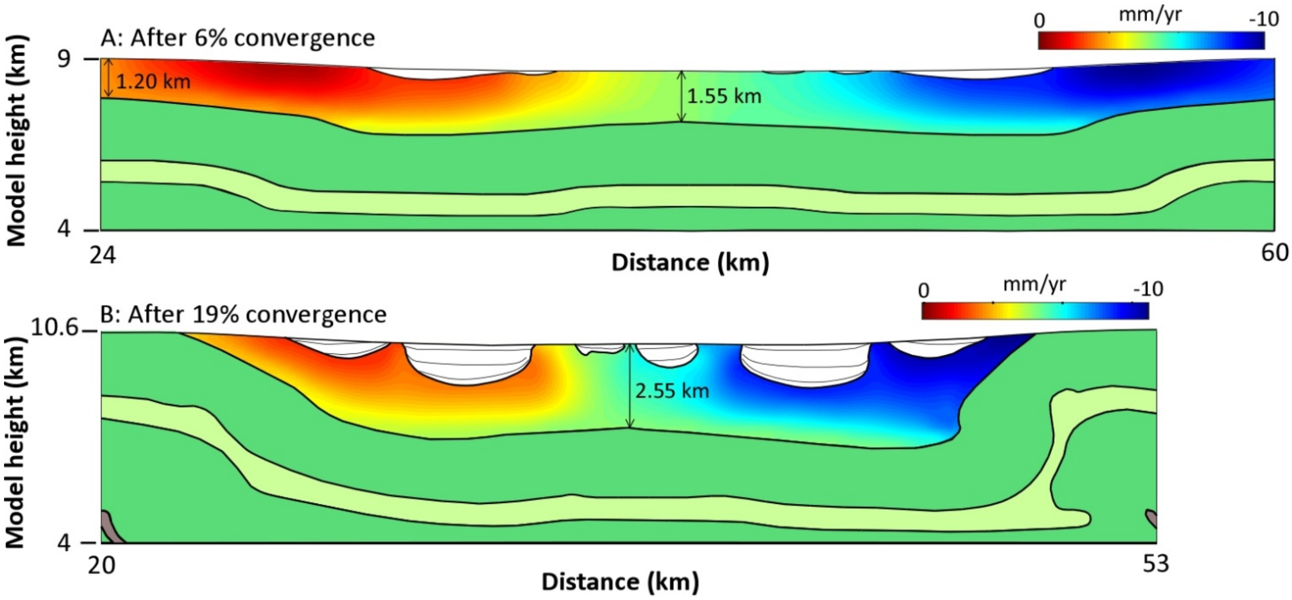
A: After 6% convergence
0
mm/yr
-10
9
4
1.20 km
1.55 km
Model height (km)
24
60
Distance (km)
B: After 19% convergence
0
mm/yr
-10
10.6
4
2.55 km
Model height (km)
20
53
Distance (km)

Fig. 17

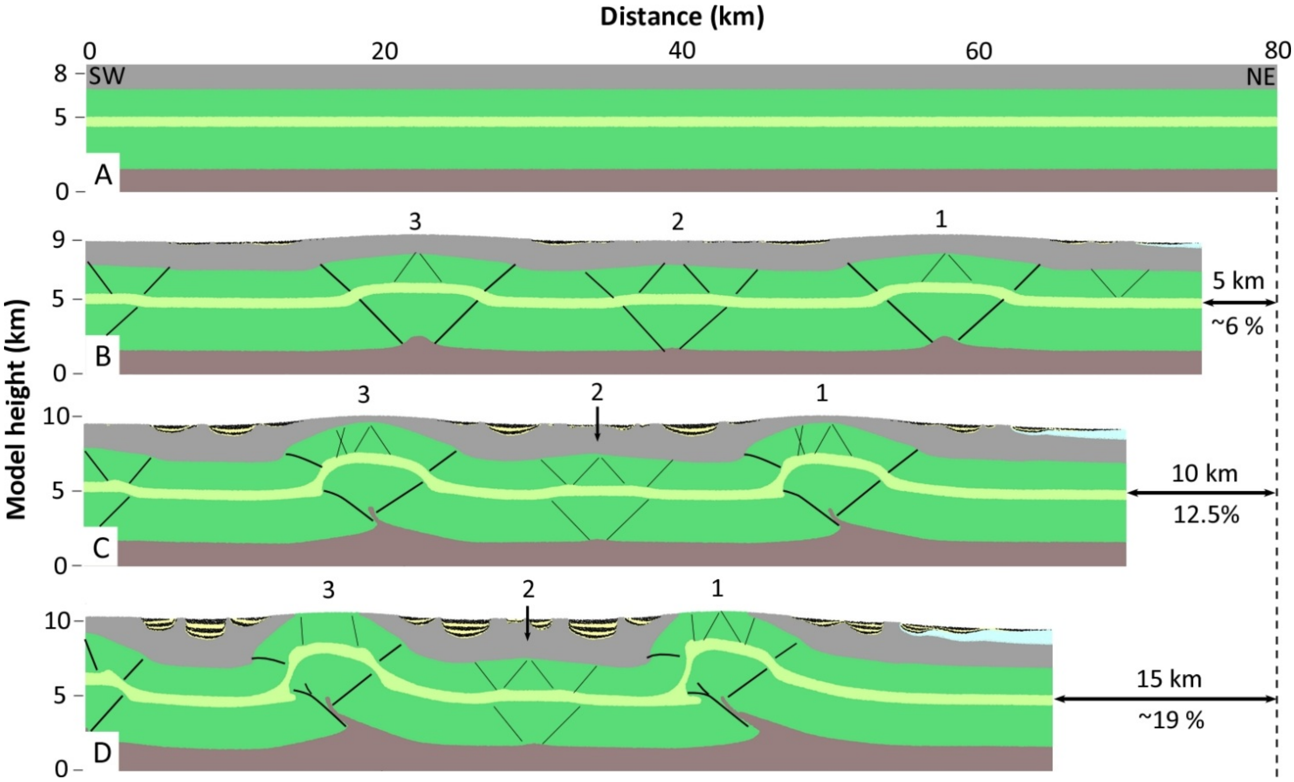
Distance (km)
0
20
40
60
80
SW
NE
Model height (km)
8
5
0
A
9
5
0
B
3
2
1
5 km
~6 %
10
5
0
C
3
2
1
10 km
12.5%
10
5
0
D
3
2
1
15 km
~19 %

Table 1- Model parameters

Model parameters		
Total thickness of rock column (km)		7-8.5
Thickness of upper detachment, T_u (km)		0.5-1.5
Thickness of intermediate detachment, T_i (km)		0.5
Thickness of basal detachment, T_b (km)		0.5-1.5
Surface coefficient, κ (m^2/s)		10^{-6} -10^{-5}
Frictional angle, ϕ (°)	Sediments	30
	Competent	30
	Detachments	---
Density, ρ (kg/m^3)	Sticky-air	1
	Sediments	2600
	Competent group	2700
	Detachments	2200
Initial viscosity, η (Pa·s)	Sticky-air	10^{17}
	Sediments	10^{25}
	Competent group	10^{25}
	Detachment	10^{18}-10^{20}
Cohesion, C (MPa)	Sediments	10^{6}
	Competent group	10^{6}
	Detachment	---

Table 2- List of the numerical models.

Model series		**Thickness of detachments (km)**			**Viscosity of detachments (Pa·s)**			**Surface process (m^2/s)**	
		Basal	Intermediate	Upper	Basal	Intermediate	Upper	Sedimentation coefficient	Erosion coefficient
model 1 (reference model)		1.5	0.5	1	10^{19}	10^{19}	10^{19}	$2 \cdot 10^{-6}$	$2 \cdot 10^{-6}$
model series 2	2a 2b 2c 2d	1.5	0.5	1	10^{19}	10^{19}	10^{19}	No surface process 10^{-6} $5 \cdot 10^{-6}$ 10^{-5}	 10^{-6} $5 \cdot 10^{-6}$ 10^{-5}
model series 3	3a 3b 3c	1.5	0.5	1	10^{19}	10^{19}	10^{19}	10^{-6} $5 \cdot 10^{-6}$ 10^{-5}	$2 \cdot 10^{-6}$
model series 4	4a 4b	0.5 1	0.5	1	10^{19}	10^{19}	10^{19}	$2 \cdot 10^{-6}$	$2 \cdot 10^{-6}$
model series 5	5a 5b	1.5	0.5	0.5 1.5	10^{19}	10^{19}	10^{19}	$2 \cdot 10^{-6}$	$2 \cdot 10^{-6}$
model series 6	6a 6b 6c	1.5	0.5	1	10^{18} $5 \cdot 10^{18}$ 10^{20}	10^{19}	10^{19}	$2 \cdot 10^{-6}$	$2 \cdot 10^{-6}$
model series 7	7a 7b 7c	1.5	0.5	1	10^{19}	10^{19}	10^{18} $5 \cdot 10^{18}$ 10^{20}	$2 \cdot 10^{-6}$	$2 \cdot 10^{-6}$

Table 3- The non-dimentional surface process diffusivity ($\tilde{\kappa}$; Simpson, 2006) calculated for model series 2 and the reference model 1.

Models	κ **(m^2/s)**	κ **(m^2/yr)**	**L (m)**	$\dot{e}$ **(1/yr)**	$\tilde{\kappa}$*
model 2b	10^{-6}	31.6			4
reference model 1	$2\cdot10^{-6}$	63.1	8000	$125\cdot10^{-9}$	8
model 2c	$5\cdot10^{-6}$	157.8			20
model 2d	10^{-5}	315.6			39

*$\tilde{\kappa} = \kappa/(L^2\dot{e})$; L= initial thickness of the layers; $\dot{e}$: initial imposed horizontal strain rate